J. Fluid Mech. (2022), *vol*. 939, A19, doi:10.1017/jfm.2022.151

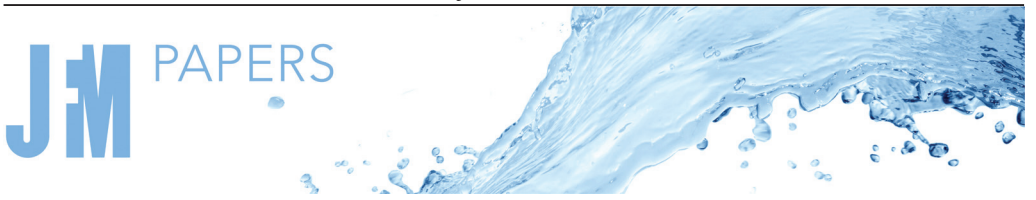

Unsteady interaction of crossflow instability with a forward-facing step

Alberto F. Rius-Vidales[1],† **and Marios Kotsonis**[1]

[1]AWEP Department, Section Aerodynamics, Delft University of Technology, Kluyverweg 1, 2629HS Delft, The Netherlands

(Received 18 August 2021; revised 30 January 2022; accepted 16 February 2022)

Experiments have been conducted on a swept wing model in a low-turbulence wind tunnel at chord Reynolds number of 2.17×10^6 to investigate the unsteady interaction of a forward-facing step (FFS) with incoming stationary crossflow (CF) vortices. The impact of varying the FFS height on the development and growth of primary and secondary CF disturbances and the ensuing laminar–turbulent transition is quantified through detailed hot-wire anemometry and infrared thermography measurements. The presence of the FFS results in either a critical (i.e. moderate transition advancement) or a supercritical behaviour (i.e. transition advancing abruptly to the FFS location). The arrival of the forced stationary CF vortices at the step is accompanied by their amplification. Unsteady analysis for the critical cases indicates temporal velocity fluctuations following closely the development of the baseline configuration (i.e. agreeing with the development of secondary instabilities). Consequently, laminar breakdown originates from the outer side of the upwelling region of the CF vortices. In contrast, for the supercritical FFS, the laminar breakdown unexpectedly originates from the inner side of the upwelling region. Evidence points to an unsteady mechanism possibly supported by locally enhanced spanwise-modulated shears and the recirculation region downstream of the FFS edge. This mechanism appears to govern the abrupt tripping of the flow in supercritical step cases. The findings in this work provide insight into the unsteady FFS–CF vortex interaction, which is pivotal to understanding the influence of an FFS on the laminar–turbulent boundary-layer transition in swept aerodynamic surfaces.

Key words: boundary layer stability, transition to turbulence

† Email address for correspondence: a.f.riusvidales@tudelft.nl

1. Introduction

The development of a three-dimensional boundary layer is intrinsic to swept aerodynamic surfaces (i.e. wing, vertical and horizontal stabilizers) on high-subsonic aircraft. Decades of research (see Reed & Saric 1989; Saric, Reed & White 2003) into these boundary layers show that the laminar–turbulent transition is determined by the unstable growth of four main instabilities: attachment-line instability; Tollmien–Schlichting (TS) waves; Görtler vortices; and crossflow (CF) vortices. An overview of the different passive and active flow control techniques to stabilize these instabilities is provided by Saric, Carpenter & Reed (2011).

Fortunately, by adequately tailoring the airfoil shape and its pressure distribution, the unstable growth of attachment-line instability, TS waves and Görtler vortices can be minimized (Saric *et al.* 2011). This leaves crossflow instability (CFI) as a critical point for predicting and controlling the laminar–turbulent transition in modern transport aircraft. Crossflow instabilities manifest as contiguous corotating vortices which develop inside the three-dimensional boundary layer in a direction closely aligned with the external inviscid flow. These vortices can remain stationary or travel along the span depending on the disturbance level outside of the boundary-layer flow (e.g. Deyhle & Bippes 1996; Downs & White 2013). A comprehensive review of the main result in the study of this instability can be found in Bippes (1999) and Saric *et al.* (2003).

Relevant to the low-turbulence level in the flight environment (see Riedel & Sitzmann 1998) is the study of stationary CF vortices (i.e. primary mode of instability). As these vortices develop, their amplitude increases until they reach a saturation level. At these conditions a highly modulated boundary-layer results, which gives rise to strong wall-normal and spanwise velocity gradients from which secondary high-frequency instabilities originate. The overall consensus in experimental (e.g. Bippes 1999; Kawakami, Kohama & Okutsu 1999; Chernoray *et al.* 2005; White & Saric 2005; Serpieri & Kotsonis 2016, 2018) and numerical (e.g. Malik, Li & Chang 1994; Högberg & Henningson 1998; Malik *et al.* 1999; Bonfigli & Kloker 2007; Groot *et al.* 2018) studies is that secondary instabilities rapidly amplify leading to the breakdown of the CF vortices and the laminar–turbulent transition.

Different active and passive flow control strategies have been proposed to stabilize the growth of the CF vortices and postpone the onset of secondary instabilities to delay the laminar–turbulent transition (e.g. Messing & Kloker 2010; Saric *et al.* 2011; Dörr & Kloker 2017; Serpieri, Yadala Venkata & Kotsonis 2017; Saric *et al.* 2019; Yadala *et al.* 2021). However, in practical applications, two-dimensional (i.e. panel joints, seals and seams) and three-dimensional (i.e. rivets, fowl and insect strikes) surface irregularities can perturb the boundary layer and advance or even abruptly force the laminar–turbulent transition. Thus, a well known limitation of laminar flow control strategies is the stringent surface smoothness requirement. The present work follows in a series of recent investigations (e.g. Rius-Vidales & Kotsonis 2020, 2021) towards understanding the effect of surface irregularities in swept wing transition. The geometries at hand are two-dimensional surface irregularities in the form of forward-facing steps (FFS) known to result in a milder destabilization of the subsonic boundary layer than its backwards-facing counterpart (Perraud & Seraudie 2000; Tufts *et al.* 2017).

A brief summary of the main research efforts towards a universal method for determining the critical FFS step height (i.e. transition advancement) in both TS and CFI dominated cases is presented in Rius-Vidales & Kotsonis (2021). Despite the wealth of information available for the study of FFS surface irregularities, only a handful focus

on three-dimensional boundary layers dominated by CFI. Consequently, the interrelation of an FFS with the primary and secondary crossflow instabilities remains a subject of ongoing investigation. Nonetheless, recent numerical (e.g. Tufts *et al.* 2017; Cooke *et al.* 2019; Casacuberta, Hickel & Kotsonis 2021) and experimental (e.g. Duncan *et al.* 2014*b*; Eppink 2018, 2020*b*; Rius-Vidales & Kotsonis 2020, 2021; Groot & Eppink 2021) studies revealed numerous unresolved aspects essential to the understanding of the FFS–CFI interaction.

In particular, Tufts *et al.* (2017) conducted a numerical investigation to support the flight and wind tunnel experiments presented by Duncan *et al.* (2014*a*,*b*) and Crawford *et al.* (2015*a*). The numerical results confirmed the experimental observations. Namely, at a low-turbulence level the addition of an FFS leads to the amplification of the primary stationary CFI. In addition, Tufts *et al.* (2017) proposed a constructive interaction between the recirculation region downstream of the FFS edge and the CF vortices as a possible mechanism for the amplification of the stationary CF disturbance. Based on this model, Tufts *et al.* (2017) suggest the use of the smooth (i.e. without FFS) CF vortices core height (y_c) estimated from a linear stability analysis as a metric to determine the step criticality (i.e. transition advancement).

Subsequent investigations by Eppink (2020*b*) and Rius-Vidales & Kotsonis (2020) on different wind tunnel models indicate that the criticality of an FFS cannot be solely determined by the step height (h) to CF vortex core-height ratio. More specifically, at a fixed step height Eppink (2020*b*) observed a considerable reduction in the extent of laminar flow when increasing the initial amplitude of the CF vortices in a previously subcritical FFS case (i.e. no transition advancement). In addition, also for a fixed FFS height, Rius-Vidales & Kotsonis (2020) identified a supercritical behaviour (i.e. abrupt transition advancement to the FFS vicinity) when forcing a late-growth mode (i.e. larger wavelength and y_c) while a subcritical behaviour was observed when forcing an early growth mode (i.e. smaller wavelength and y_c) at comparable conditions (i.e. displacement thickness (δ_h^*) and CF vortices initial amplitude). These recent findings highlight the dynamics of the FFS–CFI interaction, which are governed by the stability characteristic of the incoming CF vortices and their amplitude at the FFS.

Numerical simulations by Casacuberta *et al.* (2021) on the steady FFS–CFI interaction (i.e. simulating only stationary step-flow features) showed that as the primary CF disturbance reaches the FFS, it does not directly impinge on the step edge but instead lifts off the surface and passes over it. This behaviour is in agreement with previous experimental observations by Eppink (2020*b*) and Rius-Vidales & Kotsonis (2021). In addition, the numerical results of Casacuberta *et al.* (2021) identified a series of near-wall perturbation streaks downstream of the FFS edge developing at the spanwise wavelength of the stationary CF vortices. Given that the wavelength of these secondary perturbations coincides with the primary CF disturbance, they manifest as a secondary peak near the wall superimposed on the disturbance profile as shown in Tufts *et al.* (2017) and Eppink (2020*b*). Under certain conditions (e.g. large FFS at low-amplitude of the CF vortices) the identified near-wall peak can exceed the magnitude of the one corresponding to the primary CF disturbance. Thus, Casacuberta *et al.* (2021) propose a set of metrics to adequately determine the growth of the primary CF disturbance in these conditions.

The experiments by Eppink (2020*b*) identified the amplification of the primary CF disturbance in two regions. The first region appears to be related to a destabilization of the stationary CF vortices by the strong inflectional velocity profiles generated by the adverse pressure gradient upstream of the FFS. The second amplification region was attributed to the growth of the primary-mode harmonics by streamwise-oriented vortices originating

from the modulated recirculation region downstream of the FFS edge. Interestingly, Eppink (2020*a*,*b*) reported the occurrence of high-frequency fluctuations which coincide with the location of the shear layer of these locally separated flow. Furthermore, a detailed stability analysis by Groot & Eppink (2021) on these experiments revealed the convective nature of these unstable perturbations and identified their development on the top part of the local flow recirculation region downstream of the supercritical FFS (i.e. tripping at the step position).

Recent experiments by Rius-Vidales & Kotsonis (2021) at a higher initial amplitude also report the amplification of the stationary CF vortices at two distinct regions near the FFS. The results showed that the first amplification region is characterized by a pronounced spanwise motion of the CF vortices, potentially underlying an energy exchange mechanism due to misalignment between perturbation and base flow vectors. The second amplification region was attributed to the nominal favourable pressure gradient of the wing given that, in contrast to Eppink (2020*b*), no amplification of the primary mode by its harmonics was observed. More interestingly, Rius-Vidales & Kotsonis (2021) identified a transition delay effect for the smallest FFS case studied. This unusual behaviour resulting from the FFS–CFI interaction was attributed to a decrease in the temporal velocity fluctuations on the outer side of the upwelling region where high-frequency secondary instabilities are known to develop.

In summary, recent efforts by Eppink (2020*b*) and by the authors (Rius-Vidales & Kotsonis 2020, 2021) identify a complex dynamic relation governing the interaction between nominally stationary CF instabilities and two-dimensional FFSs. The influence of the step on the amplification of the stationary CF disturbance has received significant attention and several possible governing mechanisms have been proposed. Nevertheless, the link between the primary stationary CFI and eventual laminar breakdown is the development of secondary and unsteady disturbances in both nominally smooth and FFS cases. These considerations point out the necessity for detailed investigations on the largely unknown unsteady FFS–CFI interaction.

The objective of this work is to provide a detailed description of the unsteady interaction of CF vortices with an FFS. To this end, the laminar–turbulent transition behaviour is determined by employing infrared (IR) thermography and the development of step-induced unsteady disturbances is unveiled through high-resolution time-resolved hot-wire anemometry (HWA) measurements.

The structure of this paper is as follows. Section 2 describes the swept wing model, wind tunnel facility and measurement technique. Sections 3 and 4 provide an overview of the laminar–turbulent transition behaviour and the development of the primary CFI. Section 5 presents a detailed analysis of the development of the secondary instability of the CF vortices and step-induced unsteady disturbances. Finally, in § 6 the breakdown of the CF vortices induced by the FFS is discussed.

2. Experimental set-up and methodology

2.1. *Experimental set-up*

An experimental investigation is conducted at the Low-Turbulence Tunnel (LTT) of the Delft University of Technology to analyse the interaction of the ensuing CF vortices and an FFS irregularity on the surface of a swept wing model. The LTT is a closed return atmospheric facility designed to achieve low levels of turbulence intensity (Tu). Previous measurements by Serpieri (2018, chap. 2) at the nominal conditions corresponding to the present work ($\alpha = 3^\circ$, $Re_{c_X} = 2.17 \times 10^6$), have quantified a value of turbulence intensity

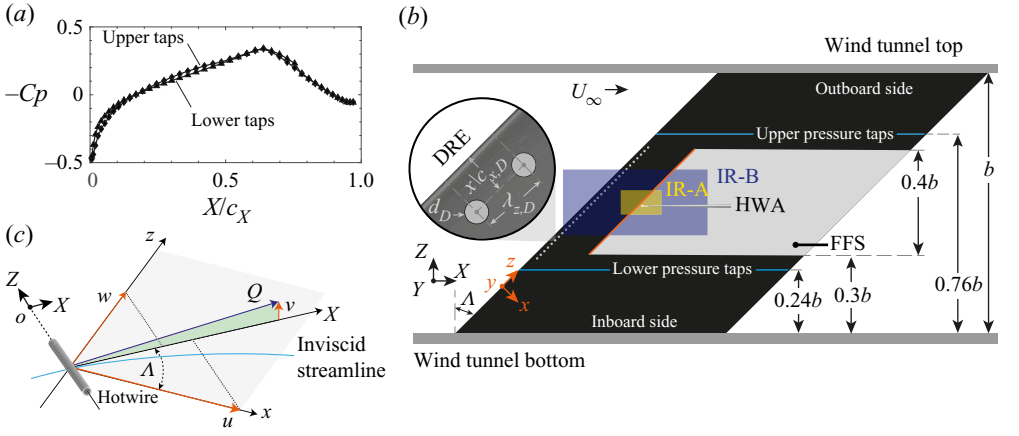

Figure 1. Experimental set-up. (*a*) Streamwise (i.e. along the X coordinate) pressure coefficient distribution on the pressure side of the model at $\alpha = 3^\circ$ and $Re_{c_X} = 2.17 \times 10^6$. (*b*) General schematic (flow direction left to right, $b = 1.25\,\mathrm{m}$ $c_X = 1.27\,\mathrm{m}$) showing the FFS (grey area), the HWA system, IR measurement domains (IR-A, IR-B) and discrete roughness elements (DRE). (*c*) Orientation of the HWA probe.

$Tu = (1/U_\infty)[(\overline{U'^2} + \overline{V'^2})/2]^{1/2} \leqslant 0.03\,\%$ (HWA measurements filtered between 2 and 5000 Hz).

The wind tunnel is furnished with an interchangeable octagonal test section (2.6 m × 1.80 m × 1.25 m, length × width × height) housing the well characterised M3J swept wing model. This model has been intensively used by the authors' research group in past and ongoing experimental investigations. The combination of this experimental facility and the swept wing model provides sufficient conditions for the experimental investigation of CFI (e.g. Serpieri & Kotsonis 2015, 2016), its control (e.g. Serpieri *et al.* 2017; Serpieri & Kotsonis 2018; Yadala *et al.* 2018, 2021) and interaction with surface irregularities (e.g. Rius-Vidales & Kotsonis 2020, 2021).

Figure 1 presents a cross-sectional view of the wind tunnel test-section. The swept wing model is mounted vertically at a sweep angle (Λ) of 45° and spans the entire height of the test-section. The Reynolds number (Re_{c_X}) used throughout is based on the corrected wind tunnel velocity ($U_\infty = 24.8\,\mathrm{m\,s^{-1}}$) and the streamwise chord length of the model corresponding to $c_X = 1.27\,\mathrm{m}$. The airfoil shape consists of a modified symmetric NACA 66018 airfoil (see Serpieri 2018, chap. 2–3). Previous measurements by Serpieri & Kotsonis (2016) have shown that at mild angles of attack ($\alpha \approx 3^\circ$) the wing model enhances the CFI while suppressing other instabilities known to occur in swept wing boundary layers such as TS waves, Görtler type instabilities, and attachment-line contamination. Due to the proximity of the HWA probe to the surface of the model, a protective film was installed on the surface.

2.1.1. *Swept wing model*

The diagram of the experimental set-up in figure 1(*b*) shows two different coordinate systems. On the first system (X, Y, Z), the streamwise X-coordinate is parallel to the wind tunnel floor and the velocity components are given, respectively, by U, V and W. In contrast, for the second system (x, y, z) the streamwise x-coordinate is normal to the leading edge of the swept wing. Note that both systems' origins coincide with the leading edge at the wing midspan.

ID	$\bar{h}$ (μm)	σ_h (μm)	x_h/c_x	δ_h^* (μm)	y_c (μm)
Clean	—	—	—	495	1115
A	346	4	0.25	—	—
B	445	3	0.25	—	—
C	708	5	0.25	—	—

Table 1. Geometrical parameters of tested configurations. For all cases nominal DREs settings are $\lambda_{z,D} = 8\,\text{mm}$, $d_D = 2\,\text{mm}$, $k_D = 200\,\mu\text{m}$, $x_D/c_x = 0.02$.

The M3J model is equipped with a total of 92 streamwise oriented (i.e. along X-coordinate) static pressure taps equally divided on the upper (outboard) and lower (inboard) side of the model as depicted on the diagram in figure 1(*b*). Note that all the measurements are conducted on the 'pressure side' of the model. Figure 1(*a*) shows the static pressure measured by the taps using a multichannel pressure scanner. The pressure distributions at $Re_{c_X} = 2.17 \times 10^6$ and $\alpha = 3^\circ$ on the outboard and inboard side of the model indicate a predominantly favourable pressure gradient (i.e. pressure minima $X/c_X \approx 0.65$). Moreover, in agreement with Serpieri & Kotsonis (2016), the validity of the infinite swept wing assumption used in the boundary-layer and stability calculations is confirmed due to the nearly identical pressure distributions on the inboard and outboard side of the wing.

From the measured pressure distribution for a clean reference case (i.e. without FFS), a numerical solution of the steady and incompressible 2.5D (i.e. spanwise invariant) laminar boundary layer is calculated along the x-coordinate. In addition, the stability of this boundary layer is determined using the Orr–Sommerfeld equation in its spatial theory formulation (see Arnal & Casalis 2000) assuming a zero spanwise growth rate due to the infinite swept wing condition.

2.1.2. *Experimental simulation of surface irregularities*

Following the strategy presented by Perraud & Seraudie (2000), Holmes *et al.* (1985) and Rius-Vidales & Kotsonis (2020, 2021), the FFS surface irregularity is simulated on the existing swept wing model using a thin flexible surface add-on. Thus, polyethylene terephthalate foils were cut to size with a CNC DCS 2500 Gerber machine and installed on the swept wing as indicated in figure 1(*b*). This study only considers FFS surface irregularities with a sharp edge (i.e. no ramp or chamfer).

During the experiments, the FFS height of each configuration was quantified *in situ* by traversing a Micro-Epsilon 2950-25 laser profilometer (reference resolution of 2 μm) along a spanwise segment of 200 mm. Table 1 presents the FFS streamwise location (x_h/c_x) and its average step height ($\bar{h}$) and standard deviation (σ_h) along the measured spanwise segment. In addition, from the aforementioned boundary-layer and stability calculations the displacement thickness (δ_h^*) and the estimated vortex core height (y_c, according to the definition by Tufts *et al.* 2017) for the forcing mode $\lambda_{z,D}$ are determined at the step location.

2.1.3. *Forcing of stationary CFI modes*

Following previous work by Rius-Vidales & Kotsonis (2020, 2021) a late-growth (i.e. with respect to the most amplified mode at the step location) is forced to study its interaction

with the FFS surface irregularity. This forcing condition is compatible with the one used by Eppink (2020*b*) albeit at a significantly higher initial amplitude. At the nominal conditions of this study, the aforementioned linear stability analysis indicates that a stationary CFI mode with a spanwise wavelength (λ_z) close to 8 mm is a late-growth CF mode ($N \approx 3.6$) with respect to the most unstable mode ($N \approx 3.9$) at the step location and is highly unstable at and downstream of the step location.

Henceforth, for all the configurations presented in table 1, stationary CF modes are conditioned using discrete roughness elements (DREs) spaced at $\lambda_{z,D} = 8$ mm. The DREs result in a narrowing of the evolving perturbations wavelength band and conditioning of the amplitude of the stationary CF modes, which destabilise the boundary-layer flow. Consequently, their use minimises potential non-uniformities in amplitude and wavelength of the CF vortices imposed by the model's micro surface roughness which can compromise the reproducibility and statistical relevance of the experiments. Therefore, DREs have proven to be an essential tool for the fundamental understanding of the development of CFI (e.g. Reibert *et al.* 1996; Saric, Carrillo & Reibert 1998; White & Saric 2005; Serpieri & Kotsonis 2016). Despite the simplifications imposed by the DREs, the fundamental interaction dynamics unveiled in these controlled cases are valuable for the understanding of cases without them.

It must be noted here that the use of DREs inherently implies the existence of intentional three-dimensional surface irregularities near the leading edge of the model. However, the term 'surface irregularity' in this work is strictly reserved for the FFS, as DREs are used only as a conditioning device and are invariantly present in all cases.

In line with Rius-Vidales & Kotsonis (2020, 2021) and Zoppini, Ragni & Kotsonis (2021), the DREs are manufactured in-house from an adhesive vinyl film using a CNC laser cutting system. In all the cases, the DREs are installed upstream of the neutral point of the forced mode. The amplitude of the DREs was chosen based on the instability regime of interest. More specifically, the present study describes the unsteady interaction of CF vortices and the step geometry. For a stationary CFI-dominated flow, it is well established that unsteady fluctuations form as secondary instabilities after saturation of the primary stationary CF vortices (e.g. White & Saric 2005). As such, in the present study, the DREs nominal height was set relatively high ($k_D = 200\,\mu$m) in order to anticipate the growth and saturation of the primary CF disturbance. This further facilitates the development of the secondary instability in both the clean and step cases while allowing for a common HWA traversing range among all tested cases.

2.2. *Measurement techniques*

2.2.1. *Infrared thermography*

The Reynolds analogy provides an effective relationship between the wall shear stress and surface heat transfer in fluids. Considering the rapid increase in skin-friction associated with the laminar–turbulent transition, IR thermography has proven to be a robust and efficient method for detecting the boundary-layer transition location in experimental studies on swept wings (e.g. Zuccher & Saric 2008; Crawford *et al.* 2015*b*; Rius-Vidales & Kotsonis 2020).

In the present work, IR thermography measurements are conducted on the pressure side of the model using two Optris PI640 IR cameras (640 px × 480 px, uncooled focal plane array, 7.5–13 μm spectral range, NETID 75 mK). The diagram on figure 1(*b*) shows the cameras' measurement region (IR-A, yellow; IR-B, blue). The first camera IR-A is equipped with a telephoto lens ($f = 41.5$ mm) to capture the near step region

(226 × 175 mm centred at $X/c_X = 0.27$ and $Z/b = 0.02$). The second camera IR-B is equipped with a wide-angle lens ($f = 10.5$ mm) to capture a larger extent of the model surface (760 × 300 mm centred at $X/c_X = 0.23$ and $Z/b = 0.04$). During the measurements seven halogen lamps (1 × 1000 W and 6 × 400 W) are positioned outside the wind tunnel test-section and used to actively heat up the model. In this active modality the lower temperatures correspond to the turbulent part while higher temperatures indicate the laminar part of the boundary-layer flow.

The extraction of the transition location from the thermal maps of camera IR-B involves using a custom-designed recognition algorithm. For each configuration tested (see table 1) a physical space transformation and distortion correction was applied to a time-averaged thermal map calculated from 50 IR images acquired at a sampling rate of 3.5 Hz. Subsequently, a differential IR thermography technique (Raffel & Merz 2014) is applied following the procedure established by Rius-Vidales & Kotsonis (2020), which considers successive measurements at increasing Reynolds numbers. The transition location is identified through a linear fit on the gradient of the binarized differential IR thermography image. Note that the confidence bands of this linear fit indicate the uniformity of the transition front (i.e. jagged or smooth), which can provide an essential insight into the dominant transition-inducing mechanism. More specifically, due to their localised nature, stationary CF vortices tend to transition in a well-defined, jagged pattern of localised wedges, while travelling disturbances essentially 'blur' the transition front reducing the spanwise variance of the transition location.

In addition to the global transition location, the thermal maps of camera IR-A provide a qualitative representation of the CF vortices' thermal footprint, from which the spatial organisation of coherent structures in the boundary layer as they interact with the FFS can be extracted. To this end, a spatial spectral analysis is performed on thermal intensity profiles extracted along the spanwise z-direction. Based on the selected camera configuration (i.e. camera location and lens) the smallest wavelength resolved according to the Nyquist limit is 0.84 mm.

2.2.2. *Hot-wire anemometry*

Recent studies from the authors (e.g. Rius-Vidales & Kotsonis 2021) as well as by Eppink (2020*b*) utilised several variations of particle image velocimetry (PIV) for a detailed reconstruction and analysis of pertinent CFI features in the vicinity of surface irregularities. A common outcome in these studies is the importance of the unsteady fluctuations in the incoming boundary layer and their relation to the surface irregularity's effect on transition. Despite a wealth of spatially correlated information extracted from optical velocimetry techniques, accurate measurement of amplitude and spectra of minute velocity fluctuations, especially in the vicinity of walls, is at best challenging. Hence, the PIV applicability towards evaluation of unsteady boundary-layer instabilities and their interaction with the FFS is limited by the sampling rate and the random and bias errors stemming from wall reflections, camera noise and laser light illumination. To this goal, the present work uses HWA as a well-established, accurate and time-resolved technique, albeit providing single-point measurements.

The boundary-layer flow measurements are conducted using a HWA probe (single wire BL probe, Dantec Dynamics 55P15) operated by a TSI IFA-300 constant temperature bridge. A custom analogue–digital (24bit) acquisition system registers and converts the HWA voltage signal to the corresponding flow velocity based on *in situ* calibration and correction for variations in atmospheric pressure and flow temperature (Hultmark & Smits 2010). The LTT wind tunnel facility is furnished with an automated traversing

system capable of translating the HWA probe (figure 1*b*) along the X, Y and Z directions with a resolution of 2.5 μm in each axis. The probe is mounted on a counterbalanced steel sting of approximately 2.5 m long. Despite the heavy construction of the sting, inevitable mechanical vibrations affecting the measurements within the characteristic resonance frequencies are detected, as will be discussed in § 5.2.1. For the entirety of measurements, the wire of the HWA probe is mounted vertically (i.e. aligned to the Z axis) and orthogonal to the X-coordinate direction as illustrated on the diagram in figure 1(*c*).

A series of wall-normal boundary-layer scans were conducted along the z-direction to form y_t–z measurement planes at different streamwise locations ($0.20 \leqslant x/c_x \leqslant 0.28$) to characterise the streamwise development of the CFI. It must be mentioned here that due to the curvature of the M3J wing, successive planes are not parallel to each other, rather normal (y_t) to the local tangent at the wall. Nonetheless, due to the large chord ($c_X = 1.27$ m) and limited measurement domain (<10 % chord), the difference in wall-tangent angle is only 1.2° between the most upstream and most downstream measurement planes. Each plane consists of 60 boundary-layer profiles equispaced in the z direction. Each profile is constructed with 40 measurement points along the wall-normal direction y_t. At each measurement point, the hot-wire signal was acquired at a sampling rate of $f_s = 51.2$ kHz for a total measurement time of two seconds. The final resolution along the z-coordinate is fixed at $\Delta z = 533$ μm while the resolution along the wall-normal direction differs per streamwise location ($60\,\mu\text{m} \leqslant \Delta y_t \leqslant 90\,\mu\text{m}$) to account for the growth in the boundary layer. For each X/c_X station, the measurement planes' starting position along the span (z^*) has been adjusted to track the evolution of three full CF vortices. Furthermore, when performing boundary-layer HWA measurements it becomes important to consider that the measurement points near the wall are being affected by spurious heat transfer to the wall, thus leading to the so-called 'tail'. Hence, it is customary to commence the measurements at a given position away from the wall and later retrieve the wall location through an extrapolation of the velocity profile (see Saric 2007). In this work, the starting position for each measurement plane is identified as the wall-normal distance for which the registered velocity reaches around 20 % of the local freestream velocity. In addition, a Taylor–Hobson microalignment telescope was used to monitor the starting distance from the wall. Finally, during post-processing the location of the wall is determined by performing a linear regression on the velocity profiles.

2.2.3. *Amplitude growth metrics*

The impact of the FFS on the stability characteristics of the CF vortices is assessed by calculating the steady and unsteady disturbance profiles from the HWA measurements acquired as indicated in § 2.2.2. Following White & Saric (2005) and Downs & White (2013) the experimental steady disturbance profile is calculated for each HWA y_t–z measurement plane as the spanwise root-mean-square of the time-average perturbation as given by (2.1). In this work the maximum ($A_M = \max(\langle\hat{q}(y_t)\rangle_z)$) of these profiles along the y_t-coordinate is non-dimensionalized with the local external velocity ($\bar{Q}_e$) and used to monitor streamwise changes in the stationary CF vortices;

$$\langle\hat{q}(y_t)\rangle_z = \sqrt{\frac{1}{n}\sum_{j=1}^{n}(\bar{Q}(y_t, z_j) - \bar{Q}_z(y_t))^2}. \tag{2.1}$$

In the typical decomposition used in linear stability analysis, the velocity perturbation (u') can be calculated by subtracting a basic state or baseflow from the measured

velocity component. In the present experiment, $\hat{q} \neq q'$, since $\bar{Q}_z(y_t)$ (used in (2.1)) corresponds to the spanwise time-average distorted flow and not to a baseflow. Nonetheless, for the experimental study of CFI, this metric has been commonly used (e.g. White & Saric 2005; Downs & White 2013; Serpieri & Kotsonis 2016).

For the study of the secondary instability, the methodology follows the one employed in White & Saric (2005), Downs & White (2013) and Serpieri & Kotsonis (2016). For each y_t–z measurement plane, a wall-normal profile is calculated by numerically integrating the temporal standard deviation (σ_Q) along the z-coordinate (i.e. spanwise direction) for every y_t position. Then, the resulting profiles are integrated along the y-coordinate to obtain the amplitude a as indicated in (2.2). This metric is used to monitor the streamwise development of unsteady disturbances;

$$a = \frac{1}{\overline{Q_e}} \frac{1}{y_t^m} \frac{1}{z^m} \int_0^{y_t^m} \int_0^{z^m} \sigma_Q(y_t, z)\, \mathrm{d}z\, \mathrm{d}y_t. \tag{2.2}$$

3. Overview of the laminar–turbulent transition behaviour

Prior to the analysis of velocity measurements in the vicinity of the FFS, this section presents the overall behaviour of the laminar–turbulent boundary-layer transition identified using IR thermography. Based on the thermal maps obtained from the IR measurements, a detailed characterization of the FFS-induced changes on the transition behaviour and spatial organization of the CF vortices is presented.

3.1. *Influence of the FFS on transition location*

The laminar–turbulent transition location is determined by monitoring changes in the model surface temperature using an IR thermographic system. For each configuration presented in table 1 thermal measurements are conducted on the pressure side of the model following the methodology described in § 2.2.1.

Figure 2 shows the thermal surface maps captured by the camera IR-B. For the clean (i.e. no FFS) forced case, the boundary-layer flow remains in a laminar state (i.e. brighter region in figure 2I*a*) for up to a third of the wing chord. Based on the methodology described in § 2.2.1 a linear fit along the span (dashed white lines in figure 2I*a*–II*b*) is calculated and the transition location extracted at the centre of the measurement domain (indicated by • markers). Figure 2(III) presents the resulting laminar–turbulent transition location for all tested configurations.

For the clean forced case the average laminar–turbulent transition location is found at $x_t/c_x \approx 0.32$. In these conditions, the dominance of the stationary CFI modes over the travelling modes is evident as the transition front pattern is not smooth (i.e. spanwise invariant transition line) but displays a series of contiguous wedges along the span. This pattern is characteristic of the breakdown process of the stationary CF vortices as indicated by Dagenhart *et al.* (1989), Bippes (1999), Saric *et al.* (2003), Downs & White (2013) and Serpieri & Kotsonis (2016). The wedged appearance of the transition front pattern is related to the thermal footprint caused by the local breakdown of contiguous stationary CF vortices. Note that the transition front along the span is slightly skewed with respect to the leading edge of the swept wing model. This behaviour is attributed to the non-uniform wind tunnel blockage that the model experiences along the test section's vertical dimension.

Following the observations presented in Rius-Vidales & Kotsonis (2020) the addition of an FFS leads to different transition behaviours classified into three different regimes.

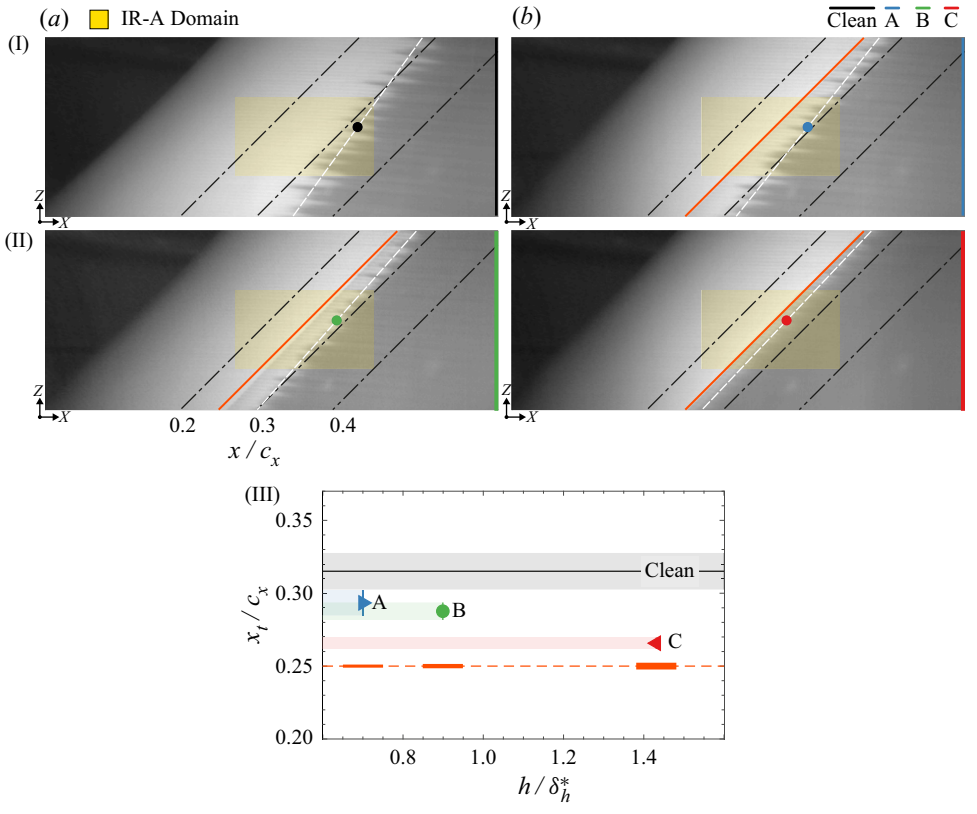

Figure 2. Thermal maps from camera IR-B (I and II, flow from left to right) and transition location (III) at $Re_{c_X} = 2.17 \times 10^6$ and $\alpha = 3^\circ$ for three different FFS (A, B and C) at fixed streamwise location (orange line denotes step location, $x_h/c_x = 0.25$). Markers (•) in I and II indicate the projection of the transition linear fit (dashed white line) to centre of the domain: (I*a*) clean; (I*b*) A; (II*a*) B; and (II*b*) C.

A subcritical regime occurs when the addition of the step results in a negligible effect on the laminar–turbulent transition process as there is nearly no change in the location of the transition front. A critical regime occurs when the addition of an FFS causes an evident and quantifiable upstream movement of the transition front. Finally, a supercritical regime occurs when the addition of an FFS results in an abrupt upstream shift of the transition front near the step location. In the latter case, the flow is said to be tripped. In this work, the addition of the two moderate FFS (case A and case B in table 1) leads to a critical regime transition behaviour, since a quantifiable upstream shift of the transition front occurs as shown in figure 2. Consequently, a further increase of the FFS height (case C in table 1) leads to a supercritical regime behaviour as the transition front occurs near the FFS, essential tripping the boundary-layer flow at its location.

3.2. *Influence of the FFS on the spatial arrangement of CF vortices*

The measurements acquired using camera IR-A (figure 1*b*) provide detailed surface temperature distributions near the FFS location as shown in figure 3. A careful inspection of the surface temperature distribution for the clean case (figure 3I*a*) reveals the thermal

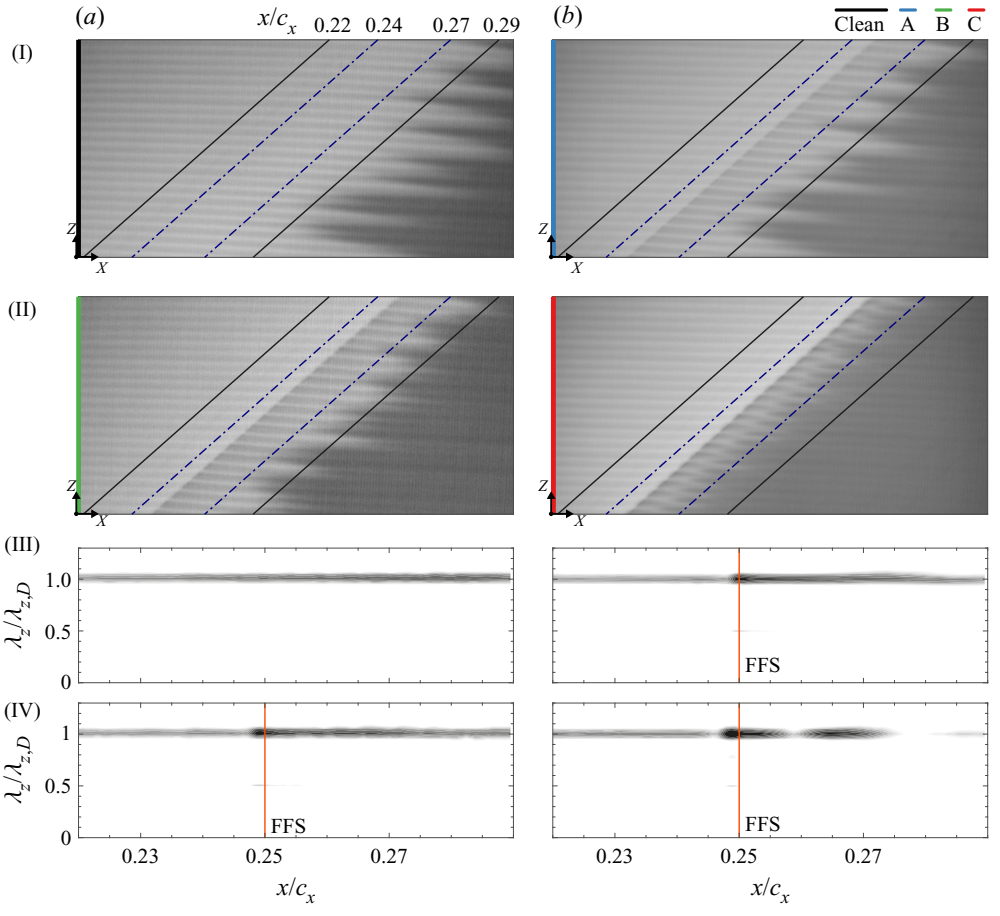

Figure 3. Thermal maps from camera IR-A (top, flow from left to right) and spectral analysis (bottom, 10 levels of $\ln(P/\bar{P}_{max_z})$ from -3 to 1): (I*a*,III*b*) clean; (I*b*-III*b*) A; (II*a*,IV*a*) B; and (II*b*,IV*b*) C. ($\lambda_{z,D} = 8$ mm.)

footprint of the CF vortices as a series of streaks nearly parallel to the streamwise X-direction alternating between high- and low-temperature values (i.e. lighter and darker).

A spatial spectral analysis is performed on a series of thermal intensity profiles extracted from the IR thermal maps along the span (i.e. along the z-direction) of the wing model to monitor changes in the spatial organization of the CF vortices. The results for the clean configuration in figure 3(III*a*) verify that the use of DREs effectively narrow down the band of stationary CFI modes active in the current boundary-layer flow since the spanwise spacing of the CF vortices matches the one forced upstream by the DREs (i.e. $\lambda_z/\lambda_{z,D} = 1$). Furthermore, figure 3(III*a*–IV*b*) indicates the persistence of the introduced wavelength even with the addition of an FFS as the forced mode dominates upstream and downstream of the step location ($x_h/c_x = 0.25$).

Previous experimental studies (e.g. Eppink 2020*b*; Rius-Vidales & Kotsonis 2020, 2021) have shown a pronounced amplification of the primary CFI mode higher harmonics at the step location. This behaviour is also observed in this work as for all the FFS cases (figure 3III*a*–IV*b*) there is a clear second peak at the step location ($x_h/c_x = 0.25$) matching the wavelength of the forced mode first higher harmonic (i.e. $\lambda_z/\lambda_{z,D} = 0.5$).

Detailed inspection of the thermal footprint for the highest FFS case (figure 3II*b*) confirm the 'fork-like' pattern previously observed in Rius-Vidales & Kotsonis (2020, 2021) associated with the supercritical regime. To further elucidate the origin of this pattern, three-dimensional flow measurements near the FFS are required. Nevertheless, one has to note the striking similarity of the identified pattern with the vortical structures presented by Eppink (2020*b*, figure 20) downstream of the step edge. In the following section, the CF vortices' streamwise development will be studied in more detail based on the HWA measurements.

4. Interaction of stationary disturbances with an FFS

The influence of the FFS on the transition location presented in § 3, indicates that for the conditions of this study (i.e. initial amplitude, step heights and freestream turbulence) the addition of an FFS leads to a reduction in the extent of the laminar flow. In this section, the HWA measurements are exploited to characterize the stationary flow interaction with the surface irregularity. This analysis covers both the stationary mean flow as well as the stationary CF instability modes.

4.1. *Influence of the FFS on the time-averaged flow*

The stationary CFI development is characterized through detailed measurements of the boundary-layer flow using an automated HWA traversing system. As described in § 2.2.2 velocity measurements are conducted in y_t–z planes (i.e. parallel to the leading edge and normal to the local model surface) at different streamwise stations in the range $0.20 \leqslant x/c_x \leqslant 0.28$. In contrast to previous experiments by Rius-Vidales & Kotsonis (2021) in which PIV was employed, the HWA signal analysed here, corresponds to the Euclidean sum, $Q = \sqrt{(u\cos\Lambda + w\sin\Lambda)^2 + v^2}$, based on the HWA probe orientation presented in figure 1(*c*).

Figure 4 presents a series of boundary-layer profiles ($\bar{Q}_z$) calculated as the spanwise average (i.e. along the z-coordinate) of the entire measurement plane. For clarity, the wall normal y_t-coordinate has been offset by the step height at its location and non-dimensionalized using the displacement thickness at the most upstream station for the clean configuration ($\delta^*_Q = 620\,\mu$m at $x/c_x = 0.22$). Upstream of the FFS location at $x/c_x = 0.24$ (figure 4I) the distortion imparted by the CF vortices on the boundary-layer flow is evident for all cases when comparing them with the numerical BL solution (dashed black line) calculated from the pressure measurements. In addition, at this position a slight deceleration which intensifies with increasing step height is evident on the boundary-layer flow (figure 4II).

Downstream of the FFS ($x/c_x \geqslant 0.256$, figure 4I) the interaction with the step leads to a more pronounced mean flow distortion as the profiles do not fully recover to the shape indicated by the clean configuration within the measurement domain. The upstream deceleration is in agreement with previous numerical and experimental studies (e.g. Duncan *et al.* 2014*a*; Tufts *et al.* 2017; Casacuberta *et al.* 2021) which indicate that the addition of an FFS leads to abrupt changes in the nominal pressure distribution in the vicinity of the step. Consequently, near the FFS location the boundary layer first experiences an adverse pressure gradient region. As the flow overcomes the apex of the FFS, it becomes influenced by a very strong favourable pressure gradient region, leading to an acceleration of the flow near the wall at ($x/c_x = 0.256$, figure 4I,II). Finally, a second adverse pressure gradient region is formed as the flow and external pressure recovers to

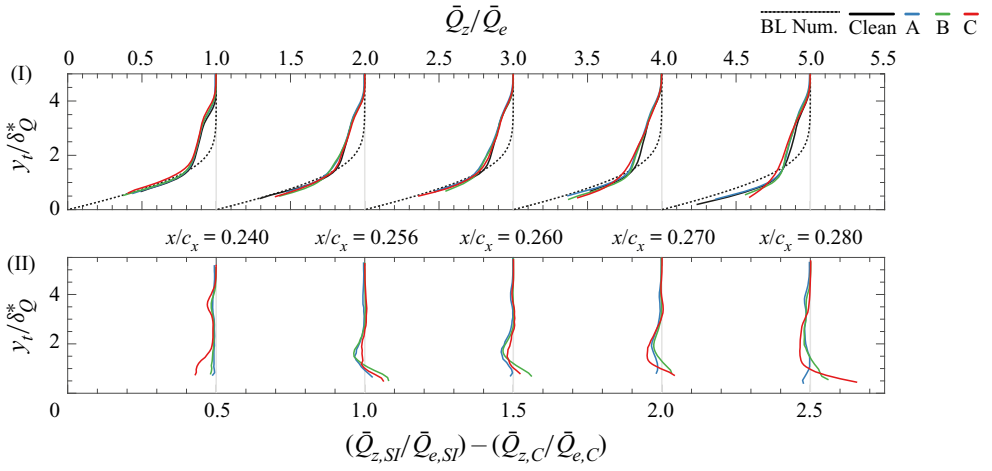

Figure 4. Selected boundary-layer profiles (I) of spanwise averaged mean flow velocity $\bar{Q}_z$ and difference (II) between these velocity profiles for the FFS cases ($\bar{Q}_{z,SI}$) and the clean configuration ($\bar{Q}_{z,C}$) upstream and downstream of the step location. Note that for visualization purposes the profiles magnitude is shifted by 1 in (I) and 0.5 in (II).

the nominal value (i.e. without FFS). This pressure modification plays an important role in determining the trajectory of the CF vortices. In particular, experiments by Eppink (2018) and Rius-Vidales & Kotsonis (2021) observed that the CF vortices experience a strong spanwise motion as they encounter the FFS. This motion requires further study as it appears to be an important aspect governing the interaction dynamics.

4.2. *Influence of the FFS on the steady disturbance*

Figure 5 presents the measured time-averaged velocity contours ($\bar{Q}$) at selected locations upstream and downstream of the FFS location. For the clean configuration (figure 5I*a*–V*a*) the velocity distribution corresponding to three stationary CF vortices is evident. The CF vortices manifest as high- and low-velocity regions evenly spaced at the spanwise wavelength forced by the DREs ($\lambda_{z,D} = 8$ mm). This correlates well with the thermal footprint and corresponding spectral analysis presented in figure 3(I*a*,III*a*).

The primary action of the corotating stationary CF vortices is to transport high-momentum fluid towards the wall (downwelling region, $\oplus$ in figure 5V*a*) and low-momentum flow away from it (upwelling region, $\ominus$ in figure 5V*a*). As the three-dimensional boundary-layer flow develops, the increase on the amplitude of the stationary CF vortices leads to a more pronounced mean flow distortion (Wassermann & Kloker 2002; White & Saric 2005; Downs & White 2013). This is particularly evident towards the downstream end of the measurement domain (figure 5V*a*).

Upon the addition of the highest FFS (case C) (figure 5I*d*–V*d*) there is a nearly immediate ($x_t/c_x \approx 0.27$) breakdown of the CF vortices leading to an anticipation of the laminar–turbulent boundary-layer transition as indicated in figure 2(III). The laminar breakdown strongly impacts the coherency and shape of the modulated boundary layer due to the increase in diffusion associated with the turbulent motion. Nevertheless, the streamwise persistence of this modulation is remarkable, as the DRE-conditioned wavelength is still visible well into the turbulent flow region (figure 3II*b*). Furthermore, particular to this FFS case, a distinct region of low-momentum fluid located

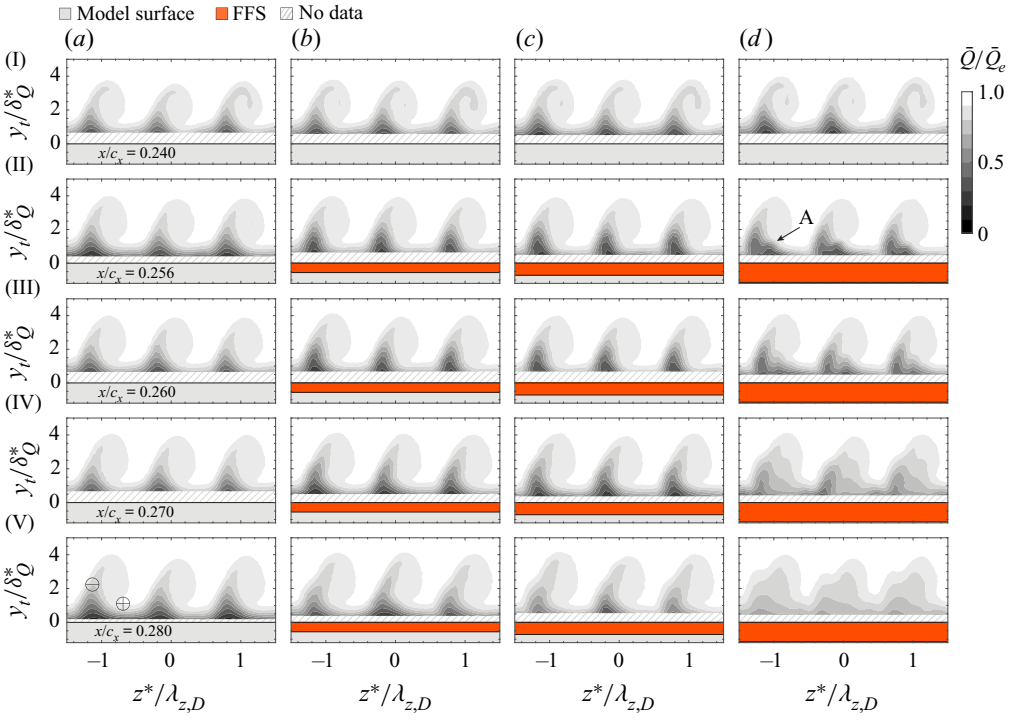

Figure 5. Contours of time-average velocity (z positive direction outboard): (*a*) clean; (*b*) A; (*c*) B, (*d*) C. ($\delta_Q^* = 620\,\mu$m and $\lambda_{z,D} = 8$ mm.)

on the inner side of the upwelling region (A in figure 5II*d*) is evident downstream of the step location.

In contrast, the addition of the smaller FFS cases (A and B in figure 5I*b*–V*c*) do not cause an immediate breakdown of the CF vortices as the laminar–turbulent boundary-layer transition occurs at $x_t/c_x \geqslant 0.28$ (figure 2III). Nonetheless, the interaction of the incoming flow with the FFS leads to an increase in the spanwise gradients on the outer side of the upwelling region, where the distance between the isovelocity contours lines reduces. Detailed studies on the development of the stationary CFI (e.g. Wassermann & Kloker 2002; White & Saric 2005; Serpieri & Kotsonis 2016) have highlighted the importance of the spanwise gradients in this region on the onset of rapidly amplifying secondary instabilities which eventually lead to the laminar–turbulent transition. The effect of these topological changes in the mean velocity gradients and fluctuations will be revisited in more detail in § 5.

Based on the time-averaged velocity fields ($\bar{Q}$) the steady disturbance profile ($\langle\hat{q}\rangle_z$) is calculated for each measurement plane following the methodology described in § 2.2.3. The resulting profiles are presented in figure 6 for selected positions upstream and downstream of the step location. Upstream of the FFS at $x/c_x = 0.240$ (figure 6I*a*) the steady disturbance profiles show two distinguishable local maxima, hereafter referred to as 'lobes'. The lower lobe (referred to as L) is located closer to the wall at $y_t/\delta_Q^* \approx 1$ and corresponds to the maxima of these profiles. The second lobe (U) is located farther away from the wall at $y_t/\delta_Q^* \approx 3$. Previous studies (e.g. Haynes & Reed 2000; White & Saric 2005) on smooth surface CF transition (i.e. without surface irregularities) have identified the appearance of the upper lobe as an indication of the nonlinear stages

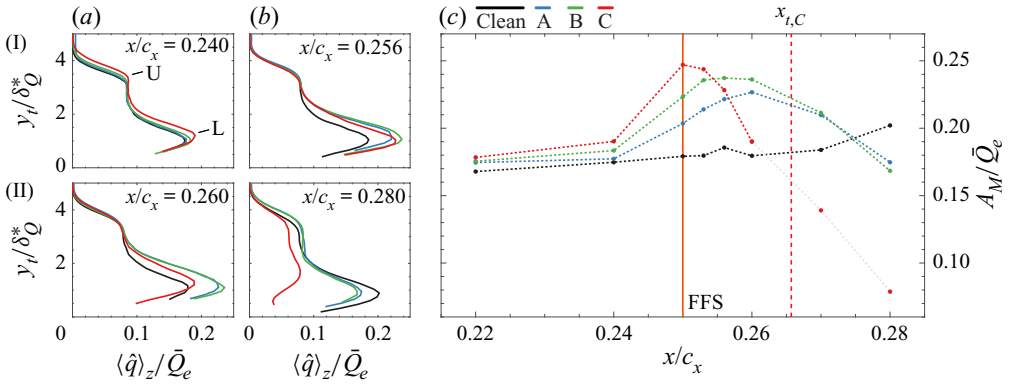

Figure 6. Selected steady disturbance $\langle\hat{q}\rangle_z$ profiles upstream and downstream of the FFS location ($\delta^*_Q = 620\,\mu$m). (*a*,*b*) Steady disturbance profiles and (*c*) streamwise evolution of the non-dimensional maximum amplitude (A_M) ($x_{t,C}$ transition location for case C).

of the CFI development. The present form of perturbation profiles reconciles well with the expectation of nonlinear development of the stationary CFI modes, given the relatively high amplitude used for the upstream forcing by the DREs. Figure 6(*c*) presents the streamwise variation of the maximum amplitude (A_M) obtained from these steady disturbance profiles. In all cases, the maximum amplitude coincides with the L lobe.

In agreement with Rius-Vidales & Kotsonis (2021) just upstream of the FFS location at $x/c_x = 0.24$ (figure 6*c*), a slight amplification of A_M for all cases is registered, reflecting the changes imparted by the step on the stability of the incoming boundary layer. Downstream of the step at $x/c_x = 0.256$ (figure 6*c*) there is a sudden increase in the amplitude of the lower lobe, which intensifies with increasing step height. Considering the highest FFS (case C), the maximum amplitude of the disturbance profile reach a value of around 25 % of the local freestream velocity $\bar{Q}_e$ at the step location ($x/c_x = 0.25$). Beyond this streamwise position the amplitude sharply decays due to the aforementioned loss of spanwise coherence prior to the laminar flow breakdown, shown in figure 5(II*d*–III*d*). Note that in figure 6(*c*) all the measurements downstream of the identified transition location (figure 2III) are connected using a grey dashed line.

For the smaller FFS (cases A and B), the maximum amplitude occurs downstream of the FFS location at $x/c_x \approx 0.256$ and 0.26, respectively. For these cases, there is only a single region of amplification prior to the detected laminar–turbulent transition at $x_t/c_x \approx 0.29$. Henceforth, this behaviour qualitatively agrees with the case C_3 in Rius-Vidales & Kotsonis (2021) corresponding to a higher FFS (C_3, $h/\delta^* = 1.30$ and $y_c/h = 1.77$) but lower initial amplitude of the CF vortices. In those conditions, the addition of the FFS resulted in anticipation of the laminar–turbulent boundary-layer transition due to an increase in the velocity fluctuations on the upwelling region's outer side. The similar transition and amplification behaviour in this study highlight the importance of the amplitude of the stationary CF vortices when reaching the FFS in determining the criticality of the step.

5. Interaction of unsteady disturbances with an FFS

As the primary stationary CF vortices develop in the boundary layer, nonlinear interactions result in amplitude saturation (Bippes 1999; Saric *et al.* 2003). This regime typically signals the onset of secondary instabilities due to the strong shears imparted on the

flow by the primary CFI. Previous numerical and experimental studies (e.g. Malik *et al.* 1994; Högberg & Henningson 1998; Kawakami *et al.* 1999; Wassermann & Kloker 2002; White & Saric 2005; Bonfigli & Kloker 2007; Serpieri & Kotsonis 2016) on stationary CFI cases without surface irregularities have connected the rapid amplification of these high-frequency secondary instabilities with the vortices breakdown and eventual laminar–turbulent transition of the boundary layer. Despite the wealth of information in smooth surface cases, the interrelation of a surface irregularity such as the present FFS with the development of unsteady disturbances remains largely unknown.

5.1. *Streamwise development of unsteady disturbances*

Previous work on boundary layers dominated by stationary CFI without surface irregularities has classified the pertinent unsteady disturbances into three main modes. Figure 7 presents the time-average velocity gradients for the clean and FFS cases to assist in their identification within the CF vortex spatial organization. The type I mode (Malik, Li & Chang 1996; Wassermann & Kloker 2002, 2003) or z-mode (Malik *et al.* 1999) is commonly located close to the local minimum of the spanwise mean flow gradient on the outer side of the upwelling region (B in figure 7III*a*). The type II mode (Malik *et al.* 1996; Wassermann & Kloker 2002, 2003) or y-mode (Malik *et al.* 1999) is commonly located away from the surface (A in figure 7I*a*) where the wall-normal gradients reach a local maximum. Finally, the type III mode (Wassermann & Kloker 2002; Bonfigli & Kloker 2007) is commonly located close to the local maxima of the spanwise gradient on the inner side of the upwelling region (C in figure 7III*a*). Note that in a stationary CFI case without surface irregularities, the temporal velocity fluctuations at type I and type II mode locations are attributed to a secondary instability of Kelvin–Helmholtz type (Bonfigli & Kloker 2007). In contrast, the velocity fluctuations corresponding to the type III mode have been traced to the nonlinear interaction between primary travelling and stationary CFI modes.

For the clean configuration, laminar–turbulent transition occurs at $x_t/c_x \approx 0.32$ as shown in figure 2(III). This behaviour correlates well with the amplitude of the primary CFI presented in figure 6(*c*), which monotonically increases in the region $x/c_x \geqslant 0.26$ reaching a level of $A_M/\bar{Q}_e \approx 0.2$ by the end of the measurement domain. This amplitude value closely matches with previous experiments by Serpieri & Kotsonis (2016) and is in agreement with typical saturation levels reported for models with 45° sweep in different wind tunnels with similar turbulence intensity levels (e.g. Downs & White 2013, figure 19).

Figure 7(III*a*–V*d*) shows the time-averaged velocity spanwise gradient (i.e. $\partial\bar{Q}/\partial z^*$) contours at selected positions downstream of the step location. Of particular interest to the development of the secondary instability corresponding to the type I mode is the increase in the negative spanwise gradient (i.e. outer side of the upwelling region, area B in figure 7III*a*) as the CF vortices amplify. Figure 7(VI) shows the streamwise evolution of the negative spanwise gradients averaged within the dashed-line regions indicated in figure 7(III*a*–V*d*). The results for the clean configuration show a slight gradual amplification of the spanwise gradients on the outer side of the upwelling region resulting from the growth of the primary instability and its nonlinear distortion on the mean flow.

In contrast, in all the FFS cases a strong amplification of $\partial\bar{Q}/\partial z^*$ on the outer side of the upwelling region occurs near the step location ($x/c_x = 0.25$ in figure 7VI). This amplification continues until a position close to where the steady perturbation (figure 6*c*) reaches its maximum value. From this point onwards a strong $\partial\bar{Q}/\partial z^*$ decay occurs due to the loss of coherence by the breakdown of the CF vortices.

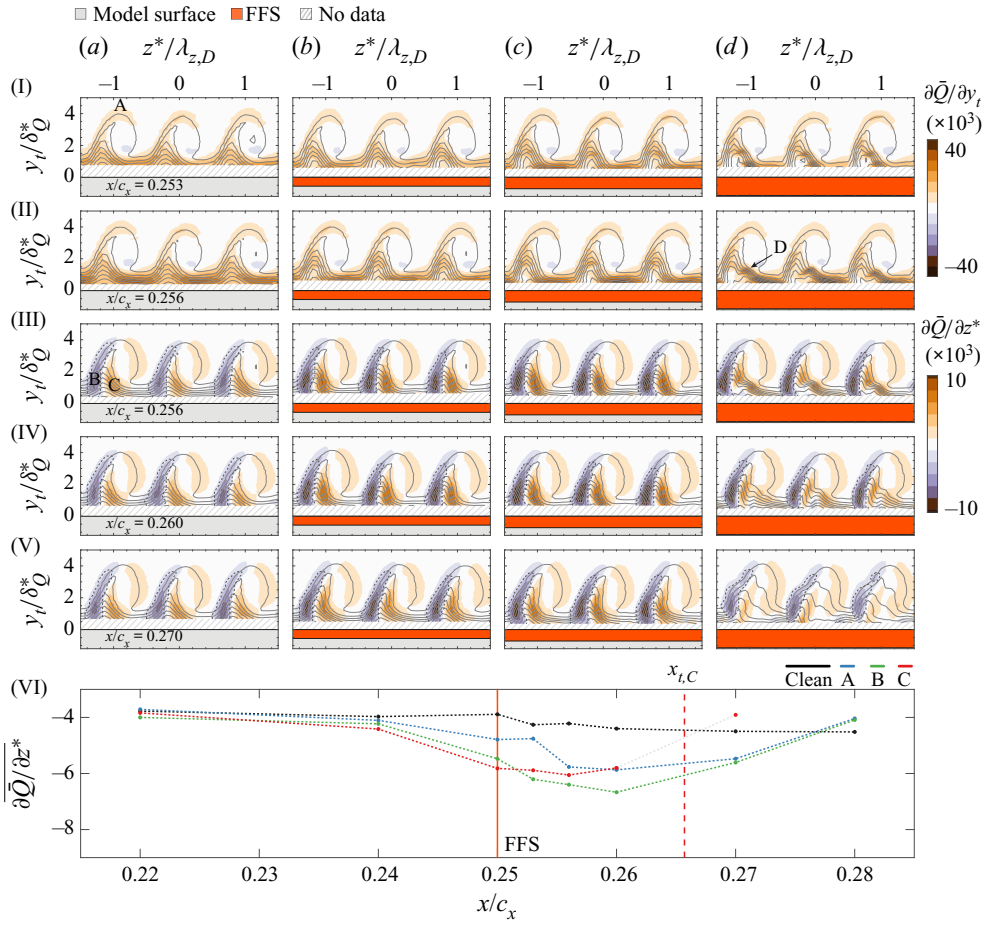

Figure 7. Contours of time-average wall-normal (I,II) and spanwise (III-V) velocity gradients and time-average velocity (grey solid lines 10 levels $\bar{Q}/\overline{Q_e}$ from 0 to 1 same contours as in figure 5): (*a*) clean; (*b*) A; (*c*) B; (*d*) C and (VI) streamwise evolution of the average spanwise gradient calculated inside the dashed line regions ($x_{t,C}$ transition location for case C, $\delta^*_Q = 620\,\mu\text{m}$ and $\lambda_{z,D} = 8\,\text{mm}$).

On the inner side of the upwelling region the organization of the spanwise ($\partial\bar{Q}/\partial z^*$) and wall-normal ($\partial\bar{Q}/\partial y_t$) gradients differ considerably between the critical (A and B) and the supercritical (C) FFS cases. In the latter, two positive spanwise gradients maxima manifest near the wall downstream of the FFS at $x/c_x = 0.256$ (figure 7III*d*). In addition, an increase in the wall-normal gradient is clearly observed (region D figure 7II*d*, local external velocity $\bar{Q}_e = 24.6\,\text{m}\,\text{s}^{-1}$) away from the wall.

Eppink (2020*a*) also identified a strong positive increase in the wall-normal gradients ($\partial U/\partial y_t$) at a similar location and attributed it to the shear layer, which develops on the top part of the flow recirculation region downstream of the FFS edge. The results from Eppink (2020*a*,*b*) showed that the recirculation downstream of the FFS is not continuous along the span but instead is highly modulated at the wavelength of the primary CFI. Thus, isolated regions of flow reversal form and develop into a complex system of streamwise vortices. Moreover, Eppink (2020*a*,*b*) reports that the formation of this flat and extended (typical height less than 300 μm and length between 7–15 mm) recirculation region downstream of the FFS edge is not only dependent on the step height but also appears to be strongly influenced by the amplitude of the primary CF disturbance.

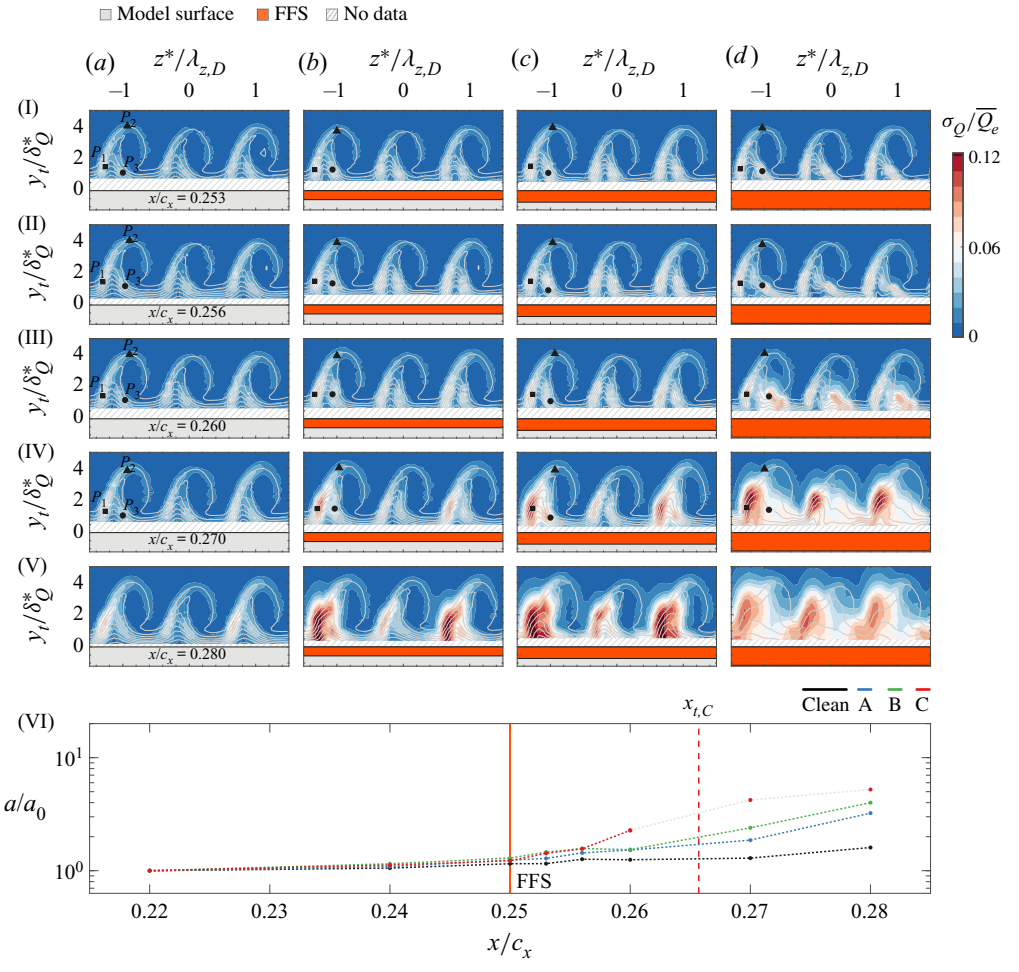

Figure 8. Contours of temporal velocity fluctuations (z positive direction outboard) and time-average velocity (grey solid lines 10 levels $\bar{Q}/\overline{Q_e}$ from 0 to 1 same contours as in figure 5): (*a*) clean; (*b*) A; (*c*) B; (*d*) C (VI); streamwise evolution of unsteady disturbance amplitude ($x_{t,C}$ transition location for case C, $\delta_Q^* = 620\,\mu$m and $\lambda_{z,D} = 8$ mm).

In this work, it is not possible to conclusively identify the recirculation regions proposed by Eppink (2020*a*,*b*) since a single wire HWA probe cannot differentiate between velocity components and their direction. Nevertheless, the qualitative agreement of the wall-normal gradients in figure 7(I*d*,II*d*) with Eppink (2020*a*, figure 7) suggests that a similar near-step flow topology occurs for the highest FFS (case C), despite the distinct spatial organization of the CF vortices presented in Eppink (2020*a*) and this work.

The spatial organisation of the total temporal velocity fluctuations (σ_Q) and the streamwise change in unsteady disturbance amplitude (a/a_0 with a_0 at $x/c_x = 0.22$) are presented in figure 8. For the clean configuration the slight increase in the unsteady disturbance amplitude (a) for $x/c_x > 0.25$ (figure 8VI) is primarily due to fluctuations on the outer side of the upwelling region (figure 8III*a*–V*a*). This behaviour is in agreement with the development of the type I secondary instability acknowledged as the driver in the breakdown of the CF vortices at similar conditions (e.g. Serpieri & Kotsonis 2018).

In the moderate FFS cases A and B, figure 8(VI), a considerable increase in amplitude occurs for $x/c_x \geqslant 0.26$. This location is slightly downstream from where the primary stationary CF disturbances reach its maximum amplification as shown in figure 6(*c*). Similar to the clean baseline configuration, the contours of σ_Q in figure 8(IV*b*–V*b*) and figure 8(IV*c*–V*c*) reveal that the increase in the temporal velocity fluctuations occurs predominantly on the outer side of the upwelling region.

Figure 8(VI) indicates that an increase in the FFS height (case C) leads to a strong amplification of the temporal velocity fluctuations downstream of the step. In this case, the interaction of the CF vortices with the FFS leads to a considerable degradation in the extent of laminar flow (i.e. supercritical regime) as the laminar–turbulent transition occurs in the vicinity of the step as shown in figure 2(II*b*,III). In contrast to the clean and the smaller FFS cases (A and B), in the higher case C an increase in temporal velocity fluctuations occurs both on the outer and inner side of the upwelling region (figure 8II*d*–IV*d*). Note that the location of the velocity fluctuations on the inner side in figure 8(II*d*) overlap with the increase in wall-normal gradients (region D in figure 7II*d*) which Eppink (2020*a*) found to be related to the localized flow recirculation region downstream of the FFS edge. The origin of these high-frequency fluctuations (at a comparable frequency to the secondary instability in their clean case) was traced to a vortex-shedding mechanism of the distorted shear-layer.

Based on the above observations, the addition of an FFS appears to lead to a notable increase in the temporal velocity fluctuations on the outer side of the upwelling region of the CF vortices in all the cases considered. The spatial location of these fluctuations suggests a dominance of the type I secondary instability mode over the type II and type III. Nevertheless, in agreement with Eppink (2020*a*,*b*) for the highest step case (C in table 1), a strong increase in the temporal velocity fluctuations also occurs on the inner side of the upwelling region. The following sections explore the development of these unsteady fluctuations to determine their effect on the breakdown of the CF vortices.

5.2. *Spatial organization of unsteady disturbances*

The analysis presented in § 5.1 showed that upon the addition of an FFS a considerable increase in the temporal velocity fluctuations (σ_Q) occurs at specific regions within the structure of the stationary CF vortices. Henceforth, a spectral analysis on the HWA time series (i.e. fluctuating velocity $Q' = Q - \bar{Q}$) is conducted at three spatial probe locations (P_1 ■; P_2 ▲; P_3 •) as indicated in figure 8(I*a*–IV*d*). The power spectral density (P) is determined for each probe signal following the averaged periodogram method (Welch 1967) using segments of 5120 samples with an overlap of 50 %. The final spectra feature a frequency resolution of $\delta_f = 10$ Hz and are non-dimensionalized following Deyhle & Bippes (1996) as $P^* = ((\delta_f P)/U_\infty^2)^{1/2}$. In addition, the entire velocity fields are bandpass filtered using a zero-phase eighth-order Butterworth filter. Note that the filtered velocity fluctuations (σ_{Q_f}) are referenced to the non-filtered external velocity ($\overline{Q_e}$) at each measurement plane. This filtering technique permits a detailed analysis of the spatial organization of the temporal velocity fluctuations on particular frequency bands as shown in Serpieri & Kotsonis (2016, 2018).

5.2.1. *Unsteady disturbances on the inner side of the CF vortices (P_3 •)*

Figure 9, shows the spectral analysis of probe P_3 (i.e. • in figure 8I*a*–IV*d* on the inner side of the upwelling region) for the measurement planes between $0.253 \leqslant x/c_x \leqslant 0.270$. In addition, to monitor the spectral content in the freestream flow, an extra probe is

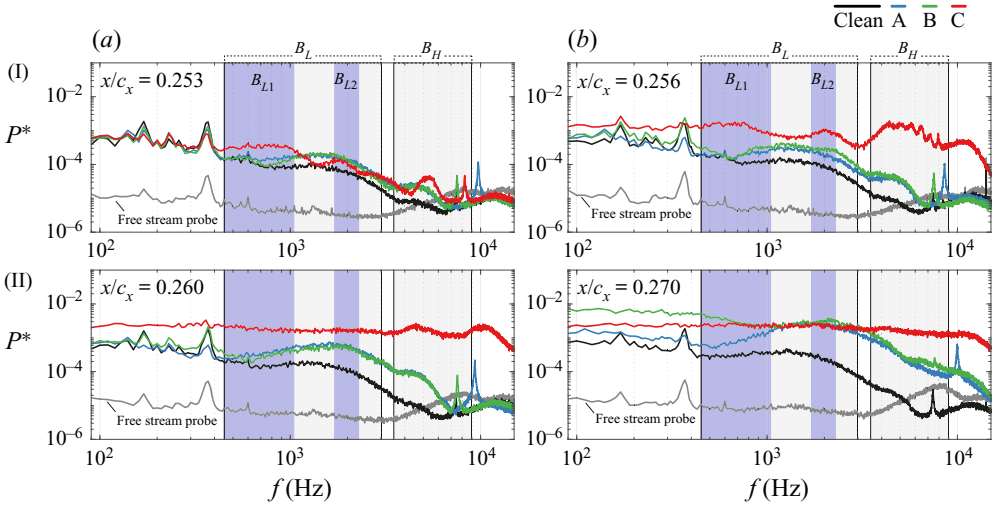

Figure 9. Spectral analysis at the inner side of the upwelling region, probe P_3 (• in figure 8) at measurement planes downstream of the step location: (I*a*) $x/c_x = 0.253$; (I*b*) $x/c_x = 0.256$; (II*a*) $x/c_x = 0.260$; and (II*b*) $x/c_x = 0.270$. Shaded grey and blue regions indicate different frequency bands.

located at the exterior of the boundary layer for the clean configuration. As anticipated, the power spectrum in the freestream is relatively flat except for two features of interest. The first one is a pair of low-frequency peaks ($f \approx 170$ and 370 Hz), which correspond to unavoidable mechanical vibrations in the supporting arm of the hot-wire probe appearing at all measurement locations. Similar to Eppink & Wlezien (2011), these probe vibrations lead to a qualitative match of the filtered velocity fluctuations (i.e. bandpass filter around the low-frequency peaks) and the topology of the time-average wall-normal velocity gradient. The second feature of interest is the high-frequency ($>10^4$ Hz) hump inherent to the HWA bridge.

Instead, inside the boundary layer at $x/c_x = 0.253$ (figure 9I*a*) the spectral analysis for the clean configuration reveals the dominance of low frequency velocity fluctuations between 450 Hz $\leqslant f \leqslant$ 3 kHz, herein this frequency band is referred to as B_L as indicated in figure 9. Although the increase of temporal velocity fluctuations at this location is in agreement with Serpieri & Kotsonis (2016, 2018) and Rius-Vidales & Kotsonis (2021), contours of the temporal velocity fluctuations filtered at the bandpass B_L (figure 10I*a*–IV*a*) show a relatively weaker development of type III modes. This is largely expected since the velocity fluctuations typically associated with the type III mode are in fact the result of the interaction between travelling and stationary CF modes. The latter is considerably stronger in the present study due to the larger amplitude associated with the DREs used at the leading edge.

When considering a critical FFS case (A and B, in table 1) an increase in the temporal velocity fluctuations with respect to the clean configuration occurs mainly inside the low-frequency band B_L as shown in figure 9. Even though the shape of the power spectrum remains similar to the clean configuration, the deviations from it in this frequency band become considerable by $x/c_x = 0.270$ (figure 9II*b*).

In contrast, the shape of the power spectrum for the supercritical FFS case (case C in table 1) differs considerably from the clean baseline. More specifically, downstream of the FFS at $x/c_x = 0.253$ and 0.256 (figure 9I*a*,I*b*) the temporal velocity fluctuations at the low frequency band B_L appear in two distinct regions B_{L1} (450 Hz $\leqslant f \leqslant$ 1050 Hz)

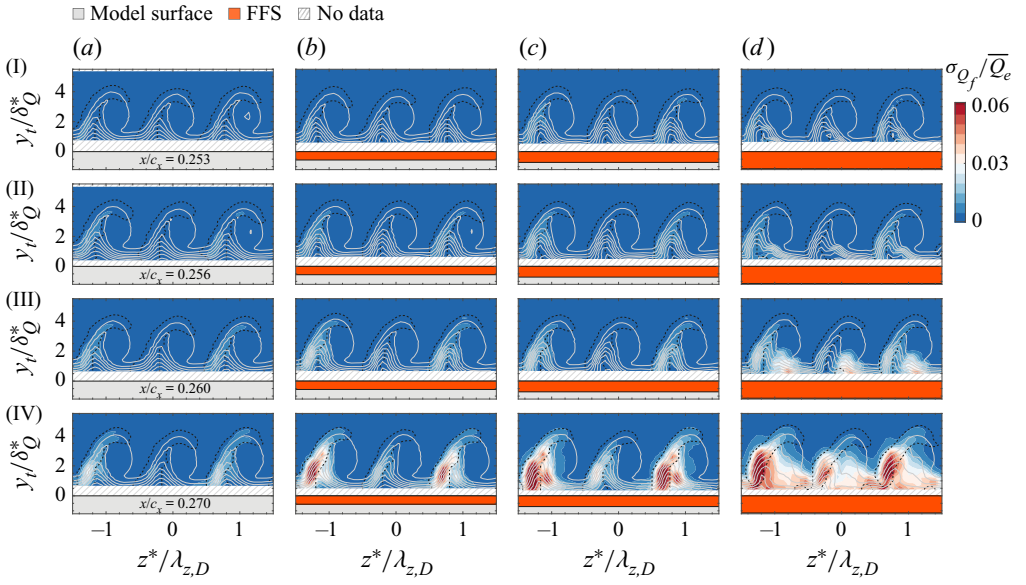

Figure 10. Bandpass filtered (B_L, 450 Hz $\leqslant f \leqslant$ 3 kHz) contours of temporal velocity fluctuations (dashed lines indicate the limit between the inner/outer side used for the calculation of a^*) and time-average velocity (grey solid lines 10 levels $\bar{Q}/\overline{Q_e}$ from 0 to 1 same contours as in figure 5): (*a*) clean, (*b*) A; (*c*) B; (*d*) C ($\delta^*_Q = 620\,\mu$m and $\lambda_{z,D} = 8$ mm).

and B_{L2} (1700 Hz $\leqslant f \leqslant$ 2300 Hz). In addition, high-frequency fluctuations appear (B_H, 3.5 kHz $\leqslant f \leqslant$ 9 kHz) as a prelude to the flattening of the power spectrum (i.e. turbulent flow) by $x/c_x = 0.260$ as shown in figure 9(II*a*).

5.2.2. *Unsteady disturbances on the outer side and cusp of the CF vortices (P_1 ■ and P_2 ▲)*

Figures 11 and 12, present the spectral analysis for the probes P_1 (i.e. ■ in figure 8 on the outer side of the upwelling region) and P_2 (i.e. ▲ in figure 8 on the top part of the CF vortices) for the measurement planes between $0.253 \leqslant x/c_x \leqslant 0.270$. In the clean configuration, the power spectrum for probe P_1 and P_2 (figures 11 and 12, respectively) indicates temporal velocity fluctuations at the high-frequency band B_H. The high-frequency content in the power spectrum at the location of these probes is in agreement with previous studies at similar conditions (e.g. Serpieri & Kotsonis 2016, 2018), which identified velocity fluctuations corresponding to a type I secondary instability mode between 3.5–6 kHz, and a type II mode between 7–8 kHz. In addition, the IR measurements in figure 2(I*a*) confirm that shortly downstream of the last HWA measurement plane, a localized breakdown (i.e. turbulent wedges) of the boundary-layer occurs as expected from the rapid development of these secondary instability modes in this case without FFS.

Consequently, the bandpass filtered contours of σ_{Q_f} at the frequency band B_H (figure 13I*a*–IV*a*) show temporal velocity fluctuations spatially located on the outer side of the upwelling region as well as top part of the CF vortices overlapping with the minimum spanwise gradients and positive wall-normal gradients shown in figure 7. This topology of temporal velocity fluctuations is typical of type I and type II modes (Serpieri & Kotsonis 2016).

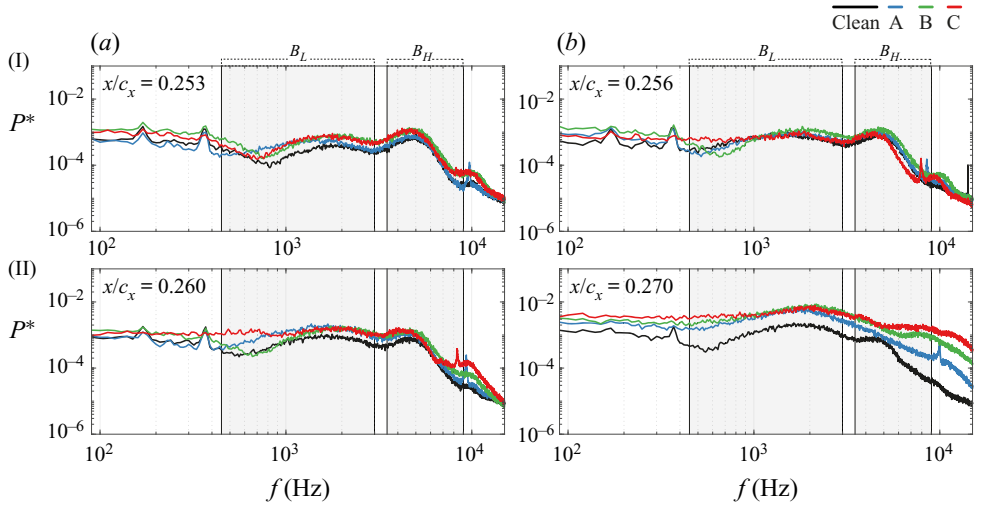

Figure 11. Spectral analysis for probe on the outer side of the upwelling region P_1 (■ in figure 8) at measurement planes downstream of the step location: (I*a*) $x/c_x = 0.253$; (I*b*) $x/c_x = 0.256$; (II*a*) $x/c_x = 0.260$; and (II*b*) $x/c_x = 0.270$. Shaded grey regions indicate different frequency bands.

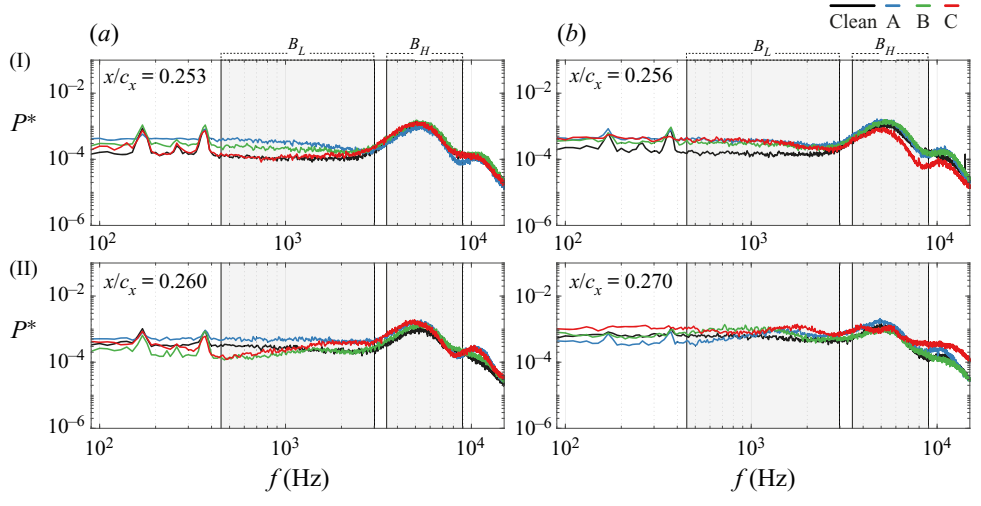

Figure 12. Spectral analysis for probe on the cusp of the CF vortex P_2 (▲ in figure 8) at measurement planes downstream of the step location: (I*a*) $x/c_x = 0.253$; (I*b*) $x/c_x = 0.256$; (II*a*) $x/c_x = 0.260$; and (II*b*) $x/c_x = 0.270$. Shaded grey regions indicate different frequency bands.

Previous numerical and experimental studies (e.g. Bonfigli & Kloker 2007; Serpieri & Kotsonis 2016, 2018) in clean (i.e. without surface irregularities) stationary CFI cases showed that type I secondary instabilities of Kelvin–Helmholtz type develop in the shear layer of the primary CFI. Therefore, the frequency of these secondary instabilities varies as they convect to higher- and lower-velocity regions in the distorted boundary layer. This behaviour manifests on the bandpass filtered velocity fluctuations at the frequency band B_L (figure 10I*a*–IV*a*), which indicate that temporal velocity fluctuations are also located on the outer side of the upwelling region at a location closer to the wall than the ones observed for the higher frequency band B_H.

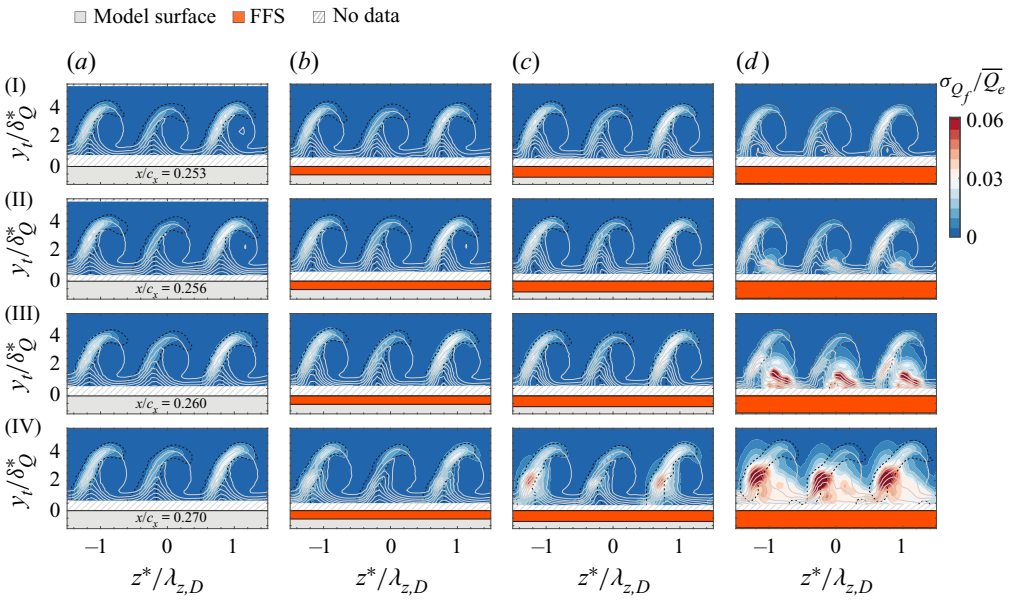

Figure 13. Bandpass filtered (B_H, 3.5 kHz $\leqslant f \leqslant$ 9 kHz) contours of temporal velocity fluctuations (dashed lines indicate the limit between the inner/outer side used for the calculation of a^*) and time-average velocity (grey solid lines 10 levels $\bar{Q}/\overline{Q_e}$ from 0 to 1 same contours as in figure 5): (*a*) clean; (*b*) A; (*c*) B; (*d*) C ($\delta_Q^* = 620\,\mu$m; and $\lambda_{z,D} = 8$ mm).

For the critical FFS cases (A and B), the spatial organization of the bandpass filtered contours of σ_{Q_f} at the low B_L (figure 10I*b*–IV*c*) and high B_H (figure 13I*b*–IV*c*) frequency bands closely matches the development of the secondary instabilities (type I and type II modes) observed in the clean configuration. A mild amplification of these fluctuations is observed as a function of step height, which is attributed to the strengthening of the stationary CF vortices and subsequent intensification of the spanwise and wall-normal shears, which drive these secondary instabilities. In contrast, in the supercritical FFS case C (figures 10I*d*–IV*d* and 13I*d*–IV*d*) the spatial distribution of the temporal velocity fluctuations strongly differ from the clean case. More specifically, downstream of the FFS (i.e. $x/c_x = 0.256$), the maximum temporal velocity fluctuations occur at the upwelling region's inner side coinciding with the location of a possible recirculation region as identified by Eppink (2020*b*). Henceforth, the nature of these fluctuations will be further investigated.

5.2.3. *Unsteady disturbances in the supercritical FFS*

The spectral analysis (figure 9I*b*) at the location of probe P_3 (i.e. • in figure 8I*d*–IV*d*) downstream of the FFS ($x/c_x = 0.256$) shows the occurrence of temporal velocity fluctuations at two distinct sub-bands B_{L1} and B_{L2}. To further investigate the origin of these unsteady disturbances, the temporal velocity fluctuations for the clean and FFS cases at this streamwise position are filtered in these frequency bands and presented in figure 14.

The spatial organization of the temporal velocity fluctuations presented in figure 14 reveals a striking difference between the supercritical FFS (case C, figure 14I*d*,II*d*) and the rest of the cases. In particular, for the clean and critical FFS cases (figure 14I*a*–II*c*), the maximum temporal velocity fluctuations are spatially located on the outer side of the upwelling region. In contrast, for the supercritical FFS the maximum fluctuations are

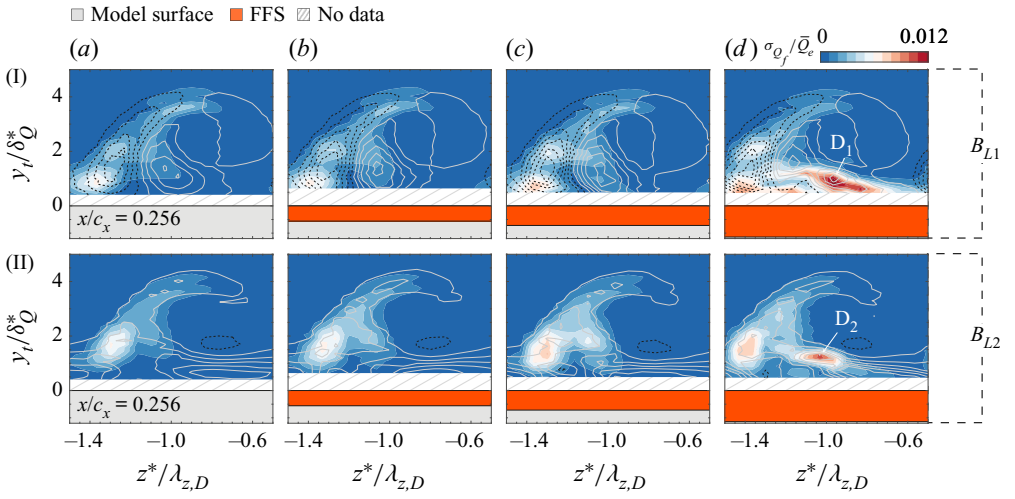

Figure 14. Bandpass filtered B_{L1}(I) (450 Hz $\leqslant f \leqslant$ 1050 Hz) and B_{L2}(II) (1700 Hz $\leqslant f \leqslant$ 2300 Hz) contours of temporal velocity fluctuations (solid contour lines indicate the positive and dashed ones negative spanwise (I) and wall-normal (II) velocity gradients, the contours corresponds to values in figure 7): (*a*) clean; (*b*) A; (*c*) B; (*d*) C ($\delta^*_Q = 620\,\mu$m and $\lambda_{z,D} = 8$ mm).

located on the inner side of the upwelling region. More importantly, for the band B_{L1} figure 14(I*d*) the maximum temporal velocity fluctuations in the supercritical FFS coincide with the second positive spanwise gradient maxima near the wall (D_1 in figure 14I*d*) while the one in the frequency band B_{L2} overlaps with the region of strong positive wall-normal gradient (D_2 in figure 14II*d*) identified as region (D) in figure 7(II*d*).

As mentioned earlier, Eppink (2020*b*) proposes that the strong positive wall-normal gradient in this region is related to the shear layer, which develops on the top of the recirculation region downstream of the FFS. Interestingly, Eppink (2020*b*) identified two distinct frequency bands at which the fluctuations in this region occur and reports that their range closely matches the one expected from flapping ($0.12U_e/L \leqslant f_F \leqslant 0.2U_e/L$, with L being the mean reattachment length) and shedding ($0.6U_e/L \leqslant f_S \leqslant 0.7U_e/L$) frequencies of separated shear layers in two-dimensional boundary layers. The qualitative agreement of the wall-normal gradients (region D on figure 7II*d*) in this work with the ones reported in Eppink (2020*a*, figure 7) indicate the possibility that a strong modulated recirculation region develops downstream of the highest FFS (case C).

Considering that the shedding of the recirculation region may occur at the peak frequency in band B_{L2} (i.e. $f_S \approx 2000$ Hz in figure 9I*b*), a rough estimation of the mean reattachment length (7.4 mm $\leqslant L_E \leqslant$ 8.6 mm) and possible flapping frequency range (343 Hz $\leqslant f_F \leqslant$ 667 Hz) is obtained for the highest FFS case based on the shedding and flapping criteria used in Eppink (2020*b*). Although the assumptions in this method are rather crude, the estimated flapping frequency range falls partially within the low-frequency band (B_{L1}, figure 9I*a*–I*b*) at which the power spectrum of the supercritical FFS (case C) strongly differs from the clean baseline one. Moreover, at this low-frequency band B_{L1} (figure 14I*d*) the maximum velocity fluctuations are also located on the inner side of the upwelling region (i.e. where flow recirculation is expected) and extend towards the wall.

Therefore, the evidence in this work points to a possible connection between the flapping/shedding mechanism described by Eppink (2020*b*) and the unsteady disturbances

on the inner side of the upwelling region for the supercritical FFS (case C). Nevertheless, the origin of the inner side fluctuations remains unclear, and particularly its relation to the mean flow deformation imparted by the step on the flow. As noted by Eppink (2020*b*) a possible recirculation region downstream of the FFS edge is not uniquely dependent on the step height but is also influenced by the amplitude of the CF vortices. Similarly, a second mechanism possibly providing the necessary velocity shears for these fluctuations could potentially be the appearance and development of near-wall Görtler vortices, due to the concave shape of the streamlines as the flow passes the step, similar to the observations presented in Marxen *et al.* (2009) in a pressure-induced laminar separation bubble. To conclusively determine the stationary and unsteady flow structure in the vicinity of the FFS, fully three-dimensional velocity measurements or numerical simulations are required.

Finally, when comparing the spectral analysis results on the inner (figure 9) and outer (figure 11) side of the upwelling region for this supercritical FFS (case C), it is clear that the power spectrum flattens first on the inner side. These results indicate that the laminar–turbulent transition for this case might not initiate on the outer side of the upwelling region as expected from the typical development of the type I secondary instability. This behaviour will be further assessed in § 6.

6. Laminar breakdown due to an FFS

The analysis of unsteady disturbances presented in § 5 indicates that the temporal velocity fluctuations for the critical FFS cases (A and B in table 1) follow closely the development observed in the clean baseline configuration. The maximum fluctuations are identified on the outer side of the upwelling region where type I secondary instabilities, widely acknowledged as the driver of the breakdown of the CF vortices, are known to develop. In contrast, when considering a supercritical FFS case (C in table 1), an entirely different behaviour results. In this case, the first evidence of laminar flow breakdown (i.e. flattening of the power-spectrum in figure 9II*a*) occurs on the inner side of the upwelling region and do not correspond to the location where the type I secondary instability commonly manifest (i.e. upwelling region's outer side). In this section, the breakdown is further examined to provide insight into the different unsteady behaviours observed in critical and supercritical FFS cases.

White & Saric (2005) and Serpieri & Kotsonis (2016, 2018) have employed the disturbance amplitude (§ 2.2.3) as a metric to monitor the development of the secondary instability modes. This approach has been particularly successful in typical CFI cases (i.e. smooth case no FFS) since the bandpass-filtered HWA measurements isolate the different unsteady modes of type I, II and III. The results in § 5 show that for the highest FFS (case C), the velocity fluctuations simultaneously occur in the outer and inner side of the upwelling region at all examined frequency bands. Thus, calculating the disturbance amplitude on the entire plane without any further processing will undesirably integrate the unsteady fluctuations of secondary instability modes of type I/II with the step-induced shedding/flapping unsteady disturbances, thus loosing oversight of their respective contributions.

To avoid this issue, the temporal velocity fluctuations occurring on the outer side and top of the upwelling region are isolated from the ones occurring on the inner side by spatially filtering the bandpass-filtered HWA measurements (figures 10, 13) based on the average velocity spanwise and wall-normal gradients (figure 7). Specifically, the boundary between the inner and outer side is defined using the overlap of the minimum spanwise

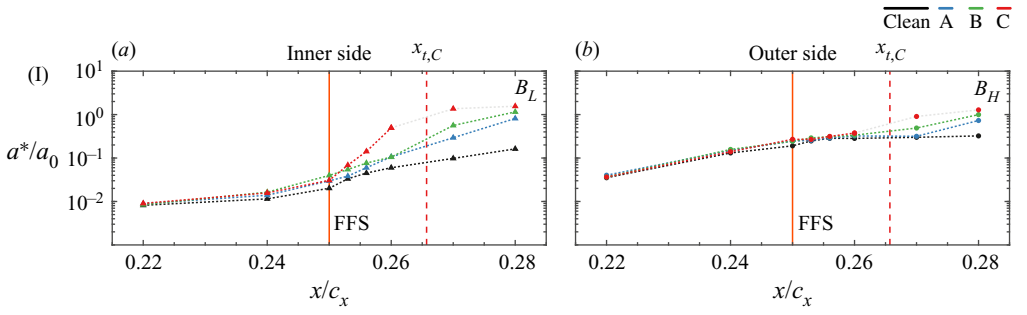

Figure 15. Unsteady disturbance amplitude a^* calculated for the inner (*a*) and outer side (*b*) of the upwelling region based on regions defined by the dashed lines for different frequency bands in figures 10 and 13: (I*a*) B_L; (I*b*) B_H ($x_{t,C}$ transition location for case C).

gradient and maximum wall-normal gradient away from the wall for each stationary CF vortex as shown by the black dashed lines in figures 10 and 13. Subsequently, the unsteady disturbance amplitude a^* is calculated on these spatially filtered measurements. Figure 15 presents the streamwise evolution of the unsteady disturbance amplitude (a^*/a_0) with the reference a_0 being taken as the total integral (i.e. no bandpass) at $x/c_x = 0.22$ for each case.

On the inner side of the upwelling region, figure 15(*a*) shows that the addition of a critical FFS case (A or B) leads to a continuous amplification of the unsteady disturbance amplitude (a^*) at the low-frequency band B_L, deviating from the trend indicated by the clean case (dashed black line). On the other hand, the fluctuations at the higher frequency band B_H on the outer side of the upwelling region (figure 15*b*) follow closely the trend dictated by the clean configuration until the primary stationary CFI in these critical FFS cases reaches its maximum amplitude ($x/c_x \approx 0.260$ in figure 6*c*). Farther downstream, an increase in the temporal velocity fluctuations at the frequency B_H corresponding to the development of type I/II secondary instabilities occurs. Detailed studies (e.g. Wassermann & Kloker 2002; White & Saric 2005; Serpieri & Kotsonis 2016; Li, Choudhari & Dua 2017) of the secondary instability in smooth cases (i.e. without FFS) showed that the development of either type I, II or the interaction of both high-frequency unsteady modes leads to the initiation of the laminar breakdown of the CF vortices.

To further quantify the origin of breakdown, the HWA measurements are high-pass filtered with a cutoff frequency of $f_c = 12$ kHz. The objective of this filtering is to isolate the increase in velocity fluctuations associated with turbulent flow from the high-frequency ones corresponding to the secondary instability modes captured by the frequency band (B_H).

The results for the critical FFS presented in figure 16(I*b*–III*c*) indicate that by the end of the measurement domain $x/c_x = 0.280$, the HWA measurements on the outer side of the upwelling region show an increase in temporal velocity fluctuations. This suggests that the origin of laminar–turbulent transition is away from the wall on the outer side of the upwelling region. This behaviour coincides with the development of a type I secondary instability mode. Therefore, the addition of a critical FFS appears to strongly amplify the primary CFI leading to the premature development of secondary instabilities, which anticipate the laminar–turbulent breakdown.

The analysis in §§ 4 and 5 showed that in the case of a supercritical FFS (case C), a strong amplification of the stationary CF vortices occurs and an increase in the temporal velocity fluctuations on both the outer and the inner side of the upwelling region, as shown

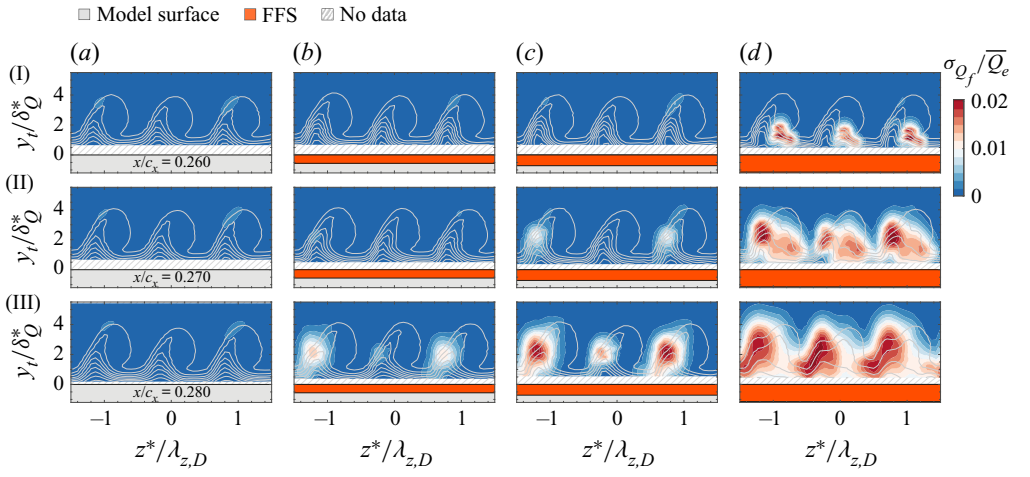

Figure 16. High-pass filtered ($f_c = 12$ kHz) contours of temporal velocity fluctuations and time-average velocity (black solid lines 10 levels from 0 to 1): (*a*) clean; (*b*) A; (*c*) B; (*d*) C ($\delta_Q^* = 620\,\mu$m and $\lambda_{z,D} = 8$ mm).

in figure 15. Nevertheless, the increase in temporal velocity fluctuations on the inner side appears to play a predominant role in the breakdown of the CF vortices, given that the spectral analysis in figure 9, showed the first indications of turbulent flow at this location.

Downstream of this supercritical FFS (case C), a strong increase in the unsteady amplitude at the low frequency bandpass B_L ($x/c_x > 0.253$ in figure 15*a*) is observed. This results are in agreement with the power spectrum shown in figure 9(I*b*), which indicates the dominance of the temporal velocity fluctuations at this frequency band. Shortly downstream, by $x/c_x = 0.260$ (figure 9II*a*), the flattening of the power spectrum (i.e. associated with turbulent flow) is observed. Instead, on the outer side of the upwelling region the flattening of the power spectrum occurs farther downstream by $x/c_x = 0.270$ as shown in the spectral analysis in figure 11(II*b*). At this location, the temporal velocity fluctuations at the higher frequencies B_H (i.e. associated type I and type II) experience a strong amplification as shown in figure 15(*b*).

Figure 16(I*d*–III*d*), shows the high-pass filtered velocity fluctuations calculated for the supercritical FFS (case C). These results confirm that the laminar–turbulent transition in this case originates first on the inner side of the upwelling region. This location coincides with a possible localized recirculation region based on the qualitative agreement with Eppink (2020*a*,*b*) described in § 5.2.3.

To this point, it is clear that the laminar–turbulent transition for the supercritical FFS does not follow the breakdown scenario of the clean and critical FFS cases. Henceforth, it is essential to determine the connection, if any, between this behaviour and the increase in temporal velocity fluctuations at the higher frequency band B_H (figure 15*b*) corresponding to secondary instabilities developing on the outer side of the upwelling region.

7. Concluding remarks

The unsteady interaction of an FFS surface irregularity with the development of CFI in the boundary layer of a swept wing model has been experimentally investigated. Decades of research into boundary layers dominated by stationary CF instability on smooth configurations identified the development of high-frequency secondary instabilities as the

unsteady mechanism responsible for driving the laminar–turbulent transition. However, the unsteady mechanisms are still not well understood when considering surface irregularities, given the intricate FFS-CFI interaction and limited published studies.

As the forced stationary CF vortices reach the FFS location, a clear amplification of the primary stationary CF disturbance is observed in all cases. Based on the step height, the ensuing laminar–turbulent transition follows either a critical regime behaviour (i.e. transition upstream of the baseline case) or a supercritical one where a substantial reduction in the extent of the laminar flow is measured as the transition occurs in the vicinity of the step.

A detailed analysis of the spatial organization and development of the temporal velocity fluctuations suggests that the unsteady mechanisms driving the laminar–turbulent transition are strongly influenced by the considered step height (i.e. critical or supercritical). For the critical FFS cases, the location and frequency content of the temporal velocity fluctuations closely follows the development of the secondary instability (type I and type II modes) observed in the clean configuration. The amplification of these fluctuations as a function of step height is attributed to the strengthening of the stationary CF vortices by the FFS and subsequent intensification of the spanwise and wall-normal shears, known to drive the secondary instability. These results confirm the impact of a critical FFS on the development of the secondary instability, previously deduced in Rius-Vidales & Kotsonis (2021) from the spatial organization of velocity disturbances at a lower amplitude of the CF vortices.

Instead, for the supercritical FFS case, the spatial and spectral distribution of the velocity fluctuations strongly differs from smaller step cases. In particular, enhanced temporal velocity fluctuations downstream of the step edge are identified in the upwelling region's inner side. These do not correspond to where secondary instability modes of type I/II commonly manifest (i.e. upwelling region's outer side) and appear at higher frequencies than typically observed for a type III mode.

A somewhat similar arrangement in the spatial organization of velocity disturbances was presented in Rius-Vidales & Kotsonis (2021) for the supercritical FFS case. Nevertheless, the lack of time-resolved measurements in Rius-Vidales & Kotsonis (2021) constrained their analysis to topology-driven inference. Although the exact origin of the unsteady disturbances in supercritical FFS cases is still elusive, evidence in this work points to a possible connection with the unsteady mechanisms related to the distorted shear-layer and/or the localized recirculation region downstream of the step edge, also identified by Eppink (2020*b*). Moreover, the qualitative agreement of velocity fluctuations and wall-normal gradients with the ones reported in Rius-Vidales & Kotsonis (2021) and Eppink (2020*a*) provides evidence that the unsteady distorted shear-layer is persistent in supercritical FFS cases at different amplitudes and spatial organization of the CF vortices.

The spectral analysis presented in this work suggests that these unsteady disturbances downstream of the supercritical FFS initiate the laminar flow breakdown. Henceforth, this work is a first step towards understanding the unsteady mechanism which triggers laminar–turbulent transition in supercritical FFS cases.

Acknowledgments. The authors would like to express their gratitude to our colleagues G. Zoppini, K. Peng, T. Michelis and J. Casacuberta for their support during the execution and discussion of the experiments. In addition, the technical guidance provided by S. Bernardy and E. Langedijk and the TU Delft Aerospace Materials and Structures Laboratory is greatly appreciated. Finally, the authors would like to acknowledge the anonymous referees for their valuable comments.

Funding. The second author would like to acknowledge the financial contribution of the European Research Council through Starting Grant 803082 'GLOWING'.

Declaration of interests. The authors report no conflict of interest.

Author ORCIDs.
Alberto F. Rius-Vidales https://orcid.org/0000-0003-4342-0278;
Marios Kotsonis https://orcid.org/0000-0003-0263-3648.

References

Arnal, D. & Casalis, G. 2000 Laminar-turbulent transition prediction in three-dimensional flows. *Prog. Aerosp. Sci.* **36** (2), 173–191.

Bippes, H. 1999 Basic experiments on transition in three-dimensional boundary layers dominated by crossflow instability. *Prog. Aerosp. Sci.* **35** (4), 363–412.

Bonfigli, G. & Kloker, M. 2007 Secondary instability of crossflow vortices: validation of the stability theory by direct numerical simulation. *J. Fluid Mech.* **583**, 229–272.

Casacuberta, J., Hickel, S. & Kotsonis, M. 2021 Mechanisms of interaction between stationary crossflow instabilities and forward-facing steps. *AIAA Paper* 2021-0854.

Chernoray, V.G., Dovgal, A.V., Kozlov, V.V. & Löfdahl, L. 2005 Experiments on secondary instability of streamwise vortices in a swept-wing boundary layer. *J. Fluid Mech.* **534**, 295–325.

Cooke, E.E., Mughal, M.S., Sherwin, S., Ashworth, R. & Rolston, S. 2019 Destabilisation of stationary and travelling crossflow disturbances due to steps over a swept wing. *AIAA Paper* 2019-3533.

Crawford, B.K., Duncan, G.T., Tufts, M.W., Saric, W.S. & Reed, H.L. 2015*a* Effects of step-excrescence location on swept-wing transition. *AIAA Paper* 2015-1233.

Crawford, B.K., Duncan, G.T., West, D.E. & Saric, W.S. 2015*b* Robust, automated processing of IR thermography for quantitative boundary-layer transition measurements. *Exp. Fluids* **56** (7), 149.

Dagenhart, J., Stack, J., Saric, W. & Mousseux, M. 1989 Crossflow-vortex instability and transition on a 45 deg swept wing. *AIAA Paper* 1989-1892.

Deyhle, H. & Bippes, H. 1996 Disturbance growth in an unstable three-dimensional boundary layer and its dependence on environmental conditions. *J. Fluid Mech.* **316**, 73–113.

Dörr, P.C. & Kloker, M.J. 2017 Crossflow transition control by upstream flow deformation using plasma actuators. *J. Appl. Phys.* **121** (6), 063303.

Downs, R.S. & White, E.B. 2013 Free-stream turbulence and the development of cross-flow disturbances. *J. Fluid Mech.* **735**, 347–380.

Duncan, G.T., Crawford, B.K., Tufts, M.W., Saric, W.S. & Reed, H.L. 2014*a* Effects of step excrescences on a swept wing in a low-disturbance wind tunnel. *AIAA Paper* 2014-0910.

Duncan, G.T., Crawford, B.K., Tufts, M.W., Saric, W.S. & Reed, H.L. 2014*b* Flight experiments on the effects of step excrescences on swept-wing transition. *Intl J. Engng Syst. Model. Simul.* **6** (3–4), 171–180.

Eppink, J.L. 2018 The effect of forward-facing steps on stationary crossflow instability growth and breakdown. *AIAA Paper* 2018-0817.

Eppink, J.L. 2020*a* High-frequency secondary instabilities downstream of a forward-facing step. *AIAA Paper* 2020-2243.

Eppink, J.L. 2020*b* Mechanisms of stationary cross-flow instability growth and breakdown induced by forward-facing steps. *J. Fluid Mech.* **897**, A15.

Eppink, J.L. & Wlezien, R. 2011 Data analysis for the nasa/boeing hybrid laminar flow control crossflow experiment. *AIAA Paper* 2011-3879.

Groot, K.J. & Eppink, J.L. 2021 Stability analysis of the flow over a swept forward-facing step using PIV base flows in a nonorthogonal coordinate system. *AIAA Paper* 2021-2908.

Groot, K.J., Serpieri, J., Pinna, F. & Kotsonis, M. 2018 Secondary crossflow instability through global analysis of measured base flows. *J. Fluid Mech.* **846**, 605–653.

Haynes, T.S. & Reed, H.L. 2000 Simulation of swept-wing vortices using nonlinear parabolized stability equations. *J. Fluid Mech.* **405**, 325–349.

Högberg, M. & Henningson, D. 1998 Secondary instability of cross-flow vortices in Falkner–Skan–Cooke boundary layers. *J. Fluid Mech.* **368**, 339–357.

Holmes, B.J., Obara, C.J., Martin, G.L. & Domack, C.S. 1985 Manufacturing tolerances for natural laminar flow airframe surfaces. SAE Technical Paper 850863.

Hultmark, M. & Smits, A.J. 2010 Temperature corrections for constant temperature and constant current hot-wire anemometers. *Meas. Sci. Technol.* **21** (10), 105404.

Kawakami, M., Kohama, Y. & Okutsu, M. 1999 Stability characteristics of stationary crossflow vortices in three-dimensional boundary layer. *AIAA Paper* 1998-811.

LI, F., CHOUDHARI, M.M. & DUA, L. 2017 Stationary crossflow breakdown due to interaction between secondary instabilities. *AIAA Paper* 2017-4302.

MALIK, M.R., LI, F. & CHANG, C.-L. 1994 Crossflow disturbances in three-dimensional boundary layers: nonlinear development, wave interaction and secondary instability. *J. Fluid Mech.* **268**, 1–36.

MALIK, M.R., LI, F. & CHANG, C.-L. 1996 Nonlinear crossflow disturbances and secondary instabilities in swept-wing boundary layers. In *IUTAM Symp. on Nonlinear Instability and Transition in Three-Dimensional Boundary Layers* (ed. P.W. Duck & P. Hall), pp. 257–266. Kluwer.

MALIK, M.R., LI, F., CHOUDHARI, M.M. & CHANG, C.-L. 1999 Secondary instability of crossflow vortices and swept-wing boundary-layer transition. *J. Fluid Mech.* **399**, 85–115.

MARXEN, O., LANG, M., RIST, U., LEVIN, O. & HENNINGSON, D.S. 2009 Mechanisms for spatial steady three-dimensional disturbance growth in a non-parallel and separating boundary layer. *J. Fluid Mech.* **634**, 165–189.

MESSING, R. & KLOKER, M.J. 2010 Investigation of suction for laminar flow control of three-dimensional boundary layers. *J. Fluid Mech.* **658**, 117–147.

PERRAUD, J. & SERAUDIE, A. 2000 Effects of steps and gaps on 2D and 3D transition. In *European Congress on Computer Methods in Applied Science and Engineering, ECCOMAS*. Paper 634.

RAFFEL, M. & MERZ, C.B. 2014 Differential infrared thermography for unsteady boundary-layer transition measurements. *AIAA J.* **52** (9), 2090–2093.

REED, H.L. & SARIC, W.S. 1989 Stability of three-dimensional boundary layers. *Annu. Rev. Fluid Mech.* **21** (1), 235–284.

REIBERT, M., SARIC, W. JR., CARRILLO, R. & CHAPMAN, K. 1996 Experiments in nonlinear saturation of stationary crossflow vortices in a swept-wing boundary layer. *AIAA Paper* 1996-0184.

RIEDEL, H. & SITZMANN, M. 1998 In-flight investigations of atmospheric turbulence. *Aerosp. Sci. Technol.* **2** (5), 301–319.

RIUS-VIDALES, A.F. & KOTSONIS, M. 2020 Influence of a forward facing step surface irregularity on swept wing transition. *AIAA J.* **58** (12), 5243–5253.

RIUS-VIDALES, A.F. & KOTSONIS, M. 2021 Impact of a forward-facing step on the development of crossflow instability. *J. Fluid Mech.* **924**, A34.

SARIC, W., CARRILLO, R. JR. & REIBERT, M. 1998 Leading-edge roughness as a transition control mechanism. *AIAA Paper* 1998-781

SARIC, W.S. 2007 Boundary-layer stability and transition. In *Springer Handbook of Experimental Fluid Mechanics* (ed. C. Tropea, A.L. Yarin & J.F. Foss), pp. 886–896. Springer.

SARIC, W.S., CARPENTER, A.L. & REED, H.L. 2011 Passive control of transition in three-dimensional boundary layers, with emphasis on discrete roughness elements. *Phil. Trans. R. Soc. Lond.* A **369** (1940), 1352–1364.

SARIC, W.S., REED, H.L. & WHITE, E.B. 2003 Stability and transition of three-dimensional boundary layers. *Annu. Rev. Fluid Mech.* **35** (1), 413–440.

SARIC, W.S., WEST, D.E., TUFTS, M.W. & REED, H.L. 2019 Experiments on discrete roughness element technology for swept-wing laminar flow control. *AIAA J.* **57** (2), 641–654.

SERPIERI, J. 2018 Cross-flow instability flow diagnostics and control of swept wing boundary layers. PhD thesis, Delft University of Technology, pp. 28–29.

SERPIERI, J. & KOTSONIS, M. 2015 Design of a swept wing wind tunnel model for study of cross-flow instability. *AIAA Paper* 2015-2576.

SERPIERI, J. & KOTSONIS, M. 2016 Three-dimensional organisation of primary and secondary crossflow instability. *J. Fluid Mech.* **799**, 200–245.

SERPIERI, J. & KOTSONIS, M. 2018 Conditioning of unsteady cross-flow instability modes using dielectric barrier discharge plasma actuators. *Exp. Therm. Fluid Sci.* **93**, 305–318.

SERPIERI, J., YADALA VENKATA, S. & KOTSONIS, M. 2017 Conditioning of cross-flow instability modes using dielectric barrier discharge plasma actuators. *J. Fluid Mech.* **833**, 164–205.

TUFTS, M.W., REED, H.L., CRAWFORD, B.K., DUNCAN, G.T. & SARIC, W.S. 2017 Computational investigation of step excrescence sensitivity in a swept-wing boundary layer. *AIAA J.* **54** (2), 602–626.

WASSERMANN, P. & KLOKER, M. 2002 Mechanisms and passive control of crossflow-vortex-induced transition in a three-dimensional boundary layer. *J. Fluid Mech.* **456**, 49–84.

WASSERMANN, P. & KLOKER, M. 2003 Transition mechanisms induced by travelling crossflow vortices in a three-dimensional boundary layer. *J. Fluid Mech.* **483**, 67–89.

WELCH, P. 1967 The use of fast Fourier transform for the estimation of power spectra: a method based on time averaging over short, modified periodograms. *IEEE Trans. Audio Electroacoust.* **15** (2), 70–73.

WHITE, E.B. & SARIC, W.S. 2005 Secondary instability of crossflow vortices. *J. Fluid Mech.* **525**, 275–308.

YADALA, S., HEHNER, M.T., SERPIERI, J., BENARD, N., DÖRR, P.C., KLOKER, M.J. & KOTSONIS, M. 2018 Experimental control of swept-wing transition through base-flow modification by plasma actuators. *J. Fluid Mech.* **844**, R2.

YADALA, S., HEHNER, M.T., SERPIERI, J., BENARD, N. & KOTSONIS, M. 2021 Plasma-based forcing strategies for control of crossflow instabilities. *AIAA J.* **59** (9), 3406–3416.

ZOPPINI, G., RAGNI, D. & KOTSONIS, M. 2021 Experimental investigation on receptivity of crossflow instability to discrete roughness amplitude and location. *AIAA Paper* 2021-052.

ZUCCHER, S. & SARIC, W.S. 2008 Infrared thermography investigations in transitional supersonic boundary layers. *Exp. Fluids* **44** (1), 145–157.